

1 A mathematical model of pan evaporation under steady 2 state conditions

3 Wee Ho Lim^{a,c,d,*}, Michael L. Roderick^{a,b,c}, Graham D. Farquhar^{a,c}

4 ^a*Research School of Biology, The Australian National University, Canberra, ACT 0200,*
5 *Australia*

6 ^b*Research School of Earth Sciences, The Australian National University, Canberra, ACT*
7 *0200, Australia*

8 ^c*Australian Research Council Centre of Excellence for Climate System Science,*
9 *Canberra, Australia*

10 ^d*Currently at: Environmental Change Institute, Oxford University Centre for the*
11 *Environment, School of Geography and the Environment, University of Oxford, Oxford*
12 *OX1 3QY, United Kingdom.*

13 Abstract

14 In the context of changing climate, global pan evaporation records have
15 shown a spatially-averaged trend of ~ -2 to ~ -3 mm a⁻² over the past 30
16 to 50 years. This global phenomenon has motivated the development of
17 the “PenPan” model (Rotstayn et al., 2006). However, the original PenPan
18 model has yet to receive an independent experimental evaluation. Hence, we
19 constructed an instrumented US Class A pan at Canberra Airport (Australia)
20 and monitored it over a three-year period (2007-2010) to uncover the physics
21 of pan evaporation under non-steady state conditions.

The experimental investigations of pan evaporation enabled theoretical
formulation and parameterisation of the aerodynamic function considering
the wind, properties of air and (with or without) the bird guard effect. The
energy balance investigation allowed for detailed formulation of the short- and
long-wave radiation associated with the albedos and the emissivities of the

*Corresponding author. Tel.: +44(0)1865 614962.
Email address: wee.ho.lim@csiro.au (Wee Ho Lim)

pan water surface and the pan wall. Here, we synthesise and generalise those earlier works to develop a new model called the “PenPan-V2” model for application under steady state conditions (i.e., uses a monthly time step). Two versions (PenPan-V2C and PenPan-V2S) are tested using pan evaporation data available across the Australian continent. Both versions outperformed the original PenPan model with better representation of both the evaporation rate and the underlying physics of a US Class A pan. The results show the improved solar geometry related calculations (e.g., albedo, area) for the pan system led to a clear improvement in representing the seasonal cycle of pan evaporation. For general applications, the PenPan-V2S is simpler and suited for applications including an evaluation of long-term trends in pan evaporation.

22 *Keywords:* pan evaporation, aerodynamic function, net irradiance,
 23 short-wave irradiance, long-wave irradiance

24 **1. Introduction**

25 Traditionally, pan evaporation measurements have been used for gauging
 26 the evaporative demand of the atmosphere over terrestrial surfaces for prac-
 27 tical applications in water resources planning and management, particularly
 28 crop irrigation scheduling (Allen et al., 1998) and open water evaporation
 29 estimation (Kohler et al., 1955). Pan evaporation networks have been estab-
 30 lished and maintained across many regions worldwide because of their sim-
 31 plicity and cost effectiveness (Stanhill, 2002). The decline in pan evaporation
 32 across many regions worldwide over the past several decades (Peterson et al.,
 33 1995) is one of the most interesting of the observed trends yet identified that

are associated in some way with climate change. It is of special interest because of its persistent decline across both energy- and water-limited regions (Roderick et al., 2009a; McVicar et al., 2012) and is concurrent with the trend of rising global averaged air temperature. This global phenomenon has attracted broad interest among the scientific community on the cause(s) and its implication(s) for the global hydrologic cycle (e.g., Peterson et al. (1995); Brutsaert and Parlange (1998); Roderick and Farquhar (2002); Ohmura and Wild (2002)). A reduction in solar irradiance (Roderick and Farquhar, 2002) and/or wind speed (Roderick et al., 2007) have been identified as the main reasons for those declines (Roderick et al., 2009b; McVicar et al., 2012).

Motivated by the prospect of utilising the long-term pan evaporation records as a scientific database for evaluating the outputs of General Circulation Models (GCMs), Rotstayn et al. (2006) combined the works of Linacre (1994) and Thom et al. (1981) to develop a steady state pan evaporation model for a US Class A pan called the “PenPan” model (Note: The two capital P’s in “PenPan” distinguish it from Linacre’s earlier contribution called “Penpan”). Using meteorological data (i.e., short-wave and long-wave radiation, air temperature, air vapour pressure, wind speed) as inputs, the original PenPan model was tested against observations in Australia (Roderick et al., 2007). However, the physical basis of the original PenPan model is limited by: (i) empirical “wind function” with limited physical understanding, (ii) single pan albedo assumption, i.e., ignoring the fact that the albedos for the pan water surface and the pan wall are different, (iii) ignoring the long-wave radiation exchange of the pan wall with its surroundings, i.e., the sky and the ground surface, (iv) the assumption that the pan is full of water whereas a

59 typical pan is partially filled (e.g., water level ~ 0.2 m for a standard US Class
60 A pan (Allen et al., 1998)). Therefore, an independent study is needed to as-
61 sess and improve the underlying physics represented by the original PenPan
62 model.

63 We constructed a highly instrumented US Class A pan that replicated
64 an operational pan at Canberra Airport in Australia to study the physics
65 of pan evaporation under non-steady state conditions. In earlier studies,
66 we performed rigorous investigations of the aerodynamics (Lim et al., 2012)
67 and energy balance (Lim et al., 2013) at our experimental pan under non-
68 steady state conditions. Here, we extend those studies through synthesising
69 and upscaling short-term process-level understanding of those formulations
70 into a model suitable for use over time periods long enough for a steady
71 state approximation to be valid (i.e., monthly). We describe the key aspects
72 of improvement of the new formulation over the original PenPan model in
73 Table 1. In Section 2, we synthesise the aerodynamic function of Lim et al.
74 (2012) and radiative formulations of Lim et al. (2013) into a Penman-type
75 combination equation. In particular, we generalise the aerodynamic function;
76 and present a new formulation of the radiative exchanges that accounts for
77 different fractional interception by the water surface relative to the external
78 walls of the pan. The new formulation is called the “PenPan-V2” model. In
79 Section 3, we describe the pan evaporation data used for model evaluation.
80 In Section 4, we evaluate two versions of model developed here (i.e., PenPan-
81 V2C for “Complete”; PenPan-V2S for “Simplified”) against observations and
82 demonstrate their advantages over the original PenPan model. In Section 5,
83 we discuss and summarise the outcomes of the research.

2. Model formulation

The central challenge in estimating wet surface evaporation is the lack of measurements. Whilst standard micrometeorological measurements (e.g., radiation, air temperature, air vapour pressure, atmospheric pressure) might be available sometimes, the temperature (or vapour pressure) of the evaporating surface is usually unavailable. To resolve this issue, the wet surface evaporation is typically formulated using an energy balance method where the surface temperature is eliminated from the underlying equations (Penman, 1948) (see simple example in Appendix A). Following that, we use the energy-balance approach to express the general equation for pan evaporation E_{pan} [m s^{-1}] under non-steady state conditions as

$$E_{pan} = \frac{(R_n - \Delta Q)}{\lambda \rho_w} - \frac{H_n}{\lambda \rho_w} \quad (1)$$

where λ [J kg^{-1}] is the latent heat of vaporisation of liquid water (~ 2.45 MJ kg^{-1}), ρ_w [kg m^{-3}] is the density of liquid water (≈ 1000 kg m^{-3}), R_n [W m^{-2}] is the net irradiance of the pan, ΔQ [W m^{-2}] is the increase in the heat storage of the bulk water and H_n [W m^{-2}] is the net sensible heat loss of the pan. An equation to calculate λ as a function of air temperature is given in Appendix B.

Following Appendix A, we expand the sensible heat term (i.e., $-\frac{H_n}{\lambda \rho_w}$) and formulate the pan evaporation E_{pan} (Eq. (1)) under steady state conditions (i.e., $\Delta Q \approx 0$). We reorganise E_{pan} into the radiative component ($E_{pan,R}$) and the aerodynamic component ($E_{pan,A}$), i.e.,

$$\begin{aligned}
E_{pan} &\approx \frac{R_n}{\lambda\rho_w} + \frac{\beta\gamma}{s + \beta\gamma} \left[f_v(e_s(T_a) - e_a(T_a)) - \frac{R_n}{\lambda\rho_w} \right] \\
&= \underbrace{\frac{s}{s + \beta\gamma} \frac{R_n}{\lambda\rho_w}}_{E_{pan,R}} + \underbrace{\frac{\beta\gamma}{s + \beta\gamma} [f_v(e_s(T_a) - e_a(T_a))]}_{E_{pan,A}}
\end{aligned} \tag{2}$$

105 where β is the ratio of heat to mass transfer coefficients of the pan, γ [Pa
 106 K^{-1}] is the psychrometric constant ($\sim 67 \text{ Pa K}^{-1}$), s [Pa K^{-1}] is the slope of
 107 the saturation vapour pressure versus temperature curve at air temperature
 108 (T_a , [K]), f_v [$\text{m s}^{-1} \text{ Pa}^{-1}$] is the aerodynamic function, $e_s(T_a)$ [Pa] is the
 109 saturated vapour pressure at the same height at which air temperature is
 110 measured, $e_a(T_a)$ [Pa] is the air vapour pressure at that same height, $E_{pan,R}$
 111 [W m^{-2}] is the radiative component of pan evaporation and $E_{pan,A}$ [W m^{-2}] is
 112 the aerodynamic component of pan evaporation. The equations to calculate
 113 s and γ are given in Appendix B. For a US Class A pan, β was previously
 114 deduced as “the ratio of the total effective surface area of the pan participat-
 115 ing in sensible heat exchange to its water surface area” and was revised from
 116 a value as large as 2.5 (Kohler et al., 1955) downward to 2.1 (Thom et al.,
 117 1981). Through the open water surface example in Appendix A (where the
 118 surface areas for both heat and mass transfer are the same), we note that
 119 the calculation of β needs to account for the fact that the thermal diffusiv-
 120 ity of air (D_h) and the diffusion coefficient for water vapour in air (D_v) are
 121 different, i.e., the ratio $\frac{D_h}{D_v} \approx 0.87$. Using the value (2.1) from Thom et al.
 122 (1981), we estimate $\beta = 2.1 \times 0.87 \approx 1.8$ and apply this value throughout
 123 this paper.

Peisker (1973) pointed out that as the evaporating water surface temperature changes, long-wave radiation losses increase in proportion with the temperature difference between water surface and the air; and that this is equivalent to an effective increase in the heat transfer coefficient compared to the vapour transfer coefficient. We have evaluated this effect and it increases $\frac{D_h}{D_v}$ by $\sim 50\%$. This effect is included in the much larger value of β which was empirically fitted by Kohler et al. (1955) and by Thom et al. (1981).

The formulations of the aerodynamic function (f_v) and the net radiation of the pan (R_n) are elucidated in the following subsections.

2.1. Aerodynamic function

Whilst presence of a boundary layer above the evaporating surface has been highlighted by early works (Penman, 1948; Giblett, 1921), we are not aware of a theoretical demonstration that shows the direct link to the widely used empirical “wind function” approach. To demonstrate that, we follow Lim et al. (2012) and express the aerodynamic function f_v as

$$f_v = \frac{M_w}{R\rho_w} \frac{D_v}{T_a} \frac{1}{\Delta z} \quad (3)$$

where M_w [kg mol⁻¹] is the molecular mass of water (=0.018 kg mol⁻¹), R [J mol⁻¹ K⁻¹] is the ideal gas constant (=8.314 J mol⁻¹ K⁻¹), D_v [m² s⁻¹] is the diffusion coefficient for water vapour in air, T_a [K] is the air temperature and Δz [m] is the boundary layer thickness. Here, $\Delta z = \left[\frac{\rho_a [(ku_{v,c})^\Phi + (nu_{ref})^\Phi]^{1/\Phi} L}{\eta_a} \right]^q L \sim \left[\frac{\rho_a [(nu_{ref})^\Phi]^{1/\Phi} L}{\eta_a} \right]^q L = \left[\frac{\rho_a (nu_{ref}) L}{\eta_a} \right]^q L$ where ρ_a [kg m⁻³] is the density of air, η_a [kg m⁻¹ s⁻¹] is the dynamic viscosity of air, $u_{v,c}$ [m s⁻¹] is the “characteristic” speed of air movement in the vertical

direction, u_{ref} [m s⁻¹] is the horizontal wind speed measured at the reference height, e.g., 2 m above ground level (u_2), L [m] is the characteristic length of the evaporating surface and (k, n, q, Φ) are the dimensionless constants ((k, n, q) range: 0 to 1; Φ range: 1 to ∞). Based on the ideal gas law, we assume that the density of air approximates that of the dry air, i.e., $\rho_a \approx \frac{P_a M_a}{RT_a}$, where P_a [Pa] is the atmospheric pressure, P_o [Pa] is the atmospheric pressure at the mean sea level (=101.3 kPa) and M_a [kg mol⁻¹] is the molecular mass of air (=0.029 kg mol⁻¹).

For a US Class A pan, we follow Lim et al. (2012, $q = -0.64$) and assume that L is the diameter (=1.21 m). We note that $D_v = 2.11 \left(\frac{T_a}{273.15} \right)^{1.94} \left(\frac{P_o}{P_a} \right) \times 10^{-5}$ m² s⁻¹ (Pruppacher and Klett, 1997) and $\eta_a = 1.8325 \left(\frac{416.16}{T_a + 120} \right) \left(\frac{T_a}{296.16} \right)^{1.5} \times 10^{-5}$ kg m⁻¹ s⁻¹ (Jacobson, 2005). With these approximations, we rearrange Eq. (3) as $f_v \approx 1.16 \frac{(T_a + 120)^{0.64}}{T_a^{0.66}} \frac{(nu_2)^{0.64}}{P_a^{0.36}} \times 10^{-8}$ m s⁻¹ Pa. For the typical range of air temperature (273.15 K $\leq T_a \leq$ 313.15 K), $\frac{(T_a + 120)^{0.64}}{T_a^{0.66}}$ varies within a narrow range from ~ 1.10 to ~ 1.13 , implying that f_v [m s⁻¹ Pa⁻¹, with u_2 in m s⁻¹ and P_a in Pa] can be approximated as

$$f_v \approx 1.3 \frac{(nu_2)^{0.64}}{P_a^{0.36}} \times 10^{-8} \quad (4)$$

The constant n is 0.1 (0.11) for a US Class A pan with (without) a bird guard (Lim et al., 2012). An equation to calculate P_a as a function of elevation above the mean sea level is given in Appendix B. Eq. (4) represents the wind function. Note that when wind speed measurements are available at a different height (e.g., 10 m), the logarithmic wind profile assumption can be applied to estimate u_2 . The shelter effect of the rim of the pan has no impact provided the pan water level is maintained between 16-20 cm above the base

169 (Chu et al., 2010); as it is in the operational pans in use in Australia. The
 170 implication is that the bulk boundary layer formulation is relevant.

171 2.2. Net irradiance

172 The net irradiance of the pan R_n consists of net short- and long-wave
 173 irradiance of the pan water surface and the pan wall, i.e.,

$$\begin{aligned} R_n &= S_n + L_n \\ &= S_{n,w} + S_{n,wall} + L_{n,w} + L_{n,wall} \end{aligned} \quad (5)$$

174 where S_n [W m^{-2}] is the net short-wave irradiance of the pan, L_n [W m^{-2}] is
 175 the net long-wave irradiance of the pan, $S_{n,w}$ [W m^{-2}] is the net short-wave
 176 irradiance of the pan water surface, $S_{n,wall}$ [W m^{-2}] is the net short-wave
 177 irradiance of the pan wall, $L_{n,w}$ [W m^{-2}] is the net long-wave irradiance of
 178 the pan water surface and $L_{n,wall}$ [W m^{-2}] is the net long-wave irradiance of
 179 the pan wall.

180 The pan water surface and the pan wall have different optical properties
 181 in the short- (albedo) and long-wave (emissivity) components. For the short-
 182 wave components, changes in the geometry of incoming solar radiation with
 183 respect to latitude and the time of the day lead to variations in the radiation
 184 intercepted by the pan wall in relation to the pan water surface thereby
 185 changing the overall albedo of the system under steady state conditions (i.e.,
 186 monthly). Hence at different latitudes and at different times of the year, the
 187 balance of contribution of the pan water surface and the pan wall towards
 188 the albedo and the net irradiance of the pan changes. Detailed formulations

189 to account for these variations within each of these terms (in Eq. (5)) are
 190 normalised to the pan water surface area (A_w) and are presented below.

191 2.2.1. Net short-wave irradiance of the pan water surface

192 The pan water surface receives short-wave radiation (global solar irradi-
 193 ance S_g which consists of beam S_b and diffuse S_d) components. The beam
 194 (S_b) is expressed as a fraction of the global solar irradiance ($f_b S_g$), while the
 195 diffuse (S_d) is the balance ($(1 - f_b) S_g$). The water in the pan is some dis-
 196 tance below the top of the pan wall and the rim (i.e, the unsubmerged part
 197 of the pan wall) casts a shadow onto the pan water surface. The extent of
 198 the shadow changes with the solar zenith angle (z) and the relative ratio of
 199 direct-to-diffuse light. With that, the pan water surface areas subjected to
 200 beam ($A_{b,w}$) and diffuse ($A_{d,w}$) irradiance are both slightly smaller than the
 201 pan water surface area (A_w). In Australia, a typical US Class A pan also has
 202 a bird guard that casts a shadow onto the pan water surface. Following Lim
 203 et al. (2013, their Eqs. (3)-(6)), we formulate the net short-wave irradiance
 204 of the pan water surface $S_{n,w}$ as

$$\begin{aligned} S_{n,w} &= (1 - \alpha'_{b,w}) \frac{S_b}{C} \frac{A'_{b,w}}{A_w} + (1 - \alpha_{d,w}) \frac{S_d}{C} \frac{A_{d,w}}{A_w} \\ &= [(1 - \alpha'_{b,w}) f_b A'_{b,w} + (1 - \alpha_{d,w}) (1 - f_b) A_{d,w}] \frac{S_g}{C A_w} \end{aligned} \quad (6)$$

205 where $\alpha'_{b,w}$ is the “effective” albedo of pan water surface subjected to beam
 206 irradiance, S_g [W m^{-2}] is the global solar irradiance, S_b [W m^{-2}] is the
 207 beam component of the global solar irradiance on a horizontal plane, C is
 208 the correction factor to account for the shading effect of the bird guard,
 209 $A'_{b,w}$ [m^2] is the “effective” area of the pan water surface subjected to beam

210 irradiance, A_w [m²] is the pan water surface area (=1.15 m²), $A_{d,w}$ [m²] is the
 211 area of the pan water surface subjected to diffuse irradiance (=1.01 m²), $\alpha_{d,w}$
 212 is the albedo of the pan water surface subjected to diffuse irradiance (=0.08)
 213 and f_b is the beam fraction of the global irradiance on a horizontal plane.
 214 We assume $C = 1.07$ for a US Class A pan with bird guard in Australia (van
 215 Dijk, 1985); $C = 1.0$ for a pan without bird guard. For monthly estimates,
 216 an equation to estimate f_b is given in Appendix B. Both $A'_{b,w}$ and $\alpha'_{b,w}$ are
 217 “effective” values of $A_{b,w}$ and $\alpha_{b,w}$ respectively which integrate the temporal
 218 variation of solar geometry in each month.

219 Over a given period (0 to τ), the estimates of $A'_{b,w}$ consider the temporal
 220 variation of $A_{b,w}$ and the cosine value of the solar zenith angle (because
 221 the pan water surface is on a horizontal plane), i.e., $A'_{b,w} = \frac{\int_0^\tau A_{b,w} \cos(z) dt}{\int_0^\tau \cos(z) dt}$.
 222 Therefore the calculation of $A'_{b,w}$ depends on the integration period τ . On
 223 an instantaneous basis, $A'_{b,w}$ equals $A_{b,w}$ because the solar zenith angle is
 224 static. On a monthly basis, $A'_{b,w}$ becomes $\frac{\overline{A_{b,w} \cos(z)}}{\overline{\cos(z)}}$ because the variation of
 225 both the numerator and denominator need to be taken into account. We
 226 assume random distribution of clouds within the day and over the month
 227 so that the transmission of solar irradiance through the atmosphere is also
 228 random. The value of $A_{b,w}$ is estimated using Lim et al. (2013, Appendix
 229 B.1); and $\cos(z)$ is estimated using the solar geometry equation $\cos(z) =$
 230 $\sin(\delta)\sin(\phi) + \cos(\delta)\cos(\phi)\cos(\omega)$ where δ is the solar declination (calculated
 231 using Roderick (1999, Appendix A)) that is assumed to be constant over the
 232 day, ϕ is the latitude and ω is the hour angle (i.e., time since the sun last
 233 passed the observer’s meridian in angular units). Note that the equation for
 234 estimating $\cos(z)$ (above) is also used to determine the hour angle at sunrise

235 and sunset (by setting the solar zenith angle to 90°). We subsequently divide
 236 the period between sunrise and sunset into 1000 equal segments and compute
 237 $A_{b,w} \cos(z)$ and $\cos(z)$ separately within each segment followed by averaging
 238 across all segments for the day. We repeat this computation procedure for all
 239 days of the month and present the monthly average of $A'_{b,w}$ over the latitude
 240 range, -60° to 60° (i.e., covering all existing US Class A pan networks) in Fig.
 241 1a. The contours resemble the ‘cosine wave’ pattern with a maximum value
 242 of about 1.085 m^2 that decline gradually as latitude increases. Therefore, if
 243 there were no rim, $A_{b,w} = A_w = 1.15 \text{ m}^2$. Our results here suggest that with
 244 minimum rim effect, $A_{b,w}$ would be around 1.085 m^2 . But $A_{b,w}$ declines to
 245 less than 1 m^2 at high latitudes and in winter.

246 We approximate the above results using a regression that accounts for
 247 the latitude and time of the year. To do that, we fitted a simple regression
 248 curve using the monthly average of $A'_{b,w}$ in March (i.e., $M=3$ in Fig. 1a),
 249 i.e.,

$$\begin{aligned}
 A'_{b,w} &\approx 1.085 - [-0.7935 \cos^3(\phi') + 1.9842 \cos^2(\phi') - 1.8325 \cos(\phi') \\
 &\quad + 0.6409] \\
 &= 0.7935 \cos^3(\phi') - 1.9842 \cos^2(\phi') + 1.8325 \cos(\phi') + 0.4441
 \end{aligned}
 \tag{7}$$

250 where $\phi' = \phi'(\phi, M) = \phi - 21.5^\circ \cos \left[\frac{360^\circ(M-6.2)}{13} \right] + 2^\circ$ and M is the middle of
 251 the month (e.g., ‘1’ for January). The calculation of ϕ' is an adjustment to
 252 account for the cosine wave contours in Fig. 1a. Here, the value ‘6.2’ means
 253 that the actual peak occurs on the June solstice (approximately 21 June,
 254 estimated as $\sim 6 + (21-15)/30 = 6.2$). The ‘13’ means that a complete annual

255 cycle of 12 gaps involves 13 points (see Fig. 1a). The ‘21.5°’ is estimated as
 256 half of 43° (the latitude difference between the peak (i.e., June solstice) and
 257 the bottom (i.e., December solstice) of each contour). The ‘+2°’ means that
 258 the maximum value occurs on -2° for $M=3$ (about six days before the March
 259 equinox). (Note that the formulation of ϕ' developed here is also applicable
 260 for the subsequent Figs 2-4.) The regression Eq. (7) qualitatively represents
 261 the general spatial and temporal pattern of $A'_{b,w}$ (cf. Fig. 1a and Fig. 1b).
 262 A quantitative assessment (Fig. 1c) suggests that Eq. (7) would adequately
 263 reproduce the seasonal cycles of the complete version (except for $A'_{b,w}$ less
 264 than 1 m² in winter at high latitudes where water in the pan would be frozen)
 265 for practical applications.

266 The albedo of pan water surface subjected to beam irradiance depends
 267 on the geometry of the solar irradiance. Over a given period (0 to τ), $\alpha'_{b,w}$
 268 consider the temporal variation of $\alpha_{b,w}$ (Lim et al., 2013, their Appendix
 269 C.1), $A_{b,w}$ (Lim et al., 2013, their Appendix B.1) and $\cos(z)$, given by
 270 $\alpha'_{b,w} = \frac{\int_0^\tau \alpha_{b,w} A_{b,w} \cos(z) dt}{\int_0^\tau A_{b,w} \cos(z) dt}$. Depending on the integration period τ , the esti-
 271 mates of $\alpha'_{b,w}$ equal $\alpha_{b,w}$ on an instantaneous basis; and becomes $\frac{\alpha_{b,w} A_{b,w} \cos(z)}{A_{b,w} \cos(z)}$
 272 over monthly time periods. Again, we assume random transmission of solar
 273 irradiance through the atmosphere. We divide the daylight period of the day
 274 into equal segments (between sunrise and sunset) similar to that described
 275 above. For each segment, we compute $\alpha_{d,w} A_{b,w} \cos(z)$ and $A_{b,w} \cos(z)$ sepa-
 276 rately and average them over the day. We repeat this computation for all
 277 days over the month and present the monthly average of $\alpha'_{b,w}$ across the same
 278 range of latitudes (as above) in Fig. 2a. The monthly average of $\alpha'_{b,w}$ has a
 279 minimum value of about 0.038 and increases gradually across the Northern

280 and Southern hemispheres. In summary, $\alpha'_{b,w} \sim 4\%$ at the equator all year
 281 round but can get beyond 10% at higher latitudes and winter.

282 Similar to above, these contour curves here resemble the ‘cosine wave’
 283 pattern over an annual cycle across all latitudes and could again be approx-
 284 imated using a regression that accounts for the latitude and time of the
 285 year. This is achieved by fitting a simple regression curve using the monthly
 286 average of $\alpha'_{b,w}$ in March (i.e., $M=3$ in Fig. 2a), given by

$$\begin{aligned}\alpha'_{b,w} &\approx 0.038 - [0.8774 \cos^3(\phi') - 2.3404 \cos^2(\phi') + 2.1401 \cos(\phi') \\ &\quad - 0.6758] \\ &= -0.8774 \cos^3(\phi') + 2.3404 \cos^2(\phi') - 2.1401 \cos(\phi') + 0.7138\end{aligned}\tag{8}$$

287 For all practical purposes, the approximation here (i.e., Eq. (8)) is capable
 288 of reproducing the general spatial and temporal pattern of $\alpha'_{b,w}$ (cf. Fig. 2a
 289 and Fig. 2b). The assessment (Fig. 2c) suggests that Eq. (8) would suit
 290 for estimating the seasonal cycles of the complete version for all practical
 291 purposes except in winter at higher latitudes (i.e., $\alpha'_{b,w}$ greater than 10%)
 292 when water in the pan is frozen.

293 2.2.2. Net short-wave irradiance of the pan wall

294 The pan wall receives short-wave radiation (beam and diffuse) from the
 295 sky and also that reflected from the surrounding ground surface. More specif-
 296 ically, Lim et al. (2013) noted that the interception of short-wave radiation
 297 at the pan wall is dominated by the section that is in contact with the pan
 298 bulk water (we describe the boundary conditions of the pan in Appendix C).

299 Following Lim et al. (2013, their Eqs. (7)-(12)), the net short-wave irradiance
 300 of the pan wall $S_{n,wall}$ is calculated as

$$\begin{aligned}
 S_{n,wall} &= (1 - \alpha'_{b,wall}) S_b \tan(z)' \frac{A_{b,wall}}{A_w} + (1 - \alpha_{d,wall}) \frac{S_d}{2} \frac{A_{d,wall}}{A_w} \\
 &\quad + (1 - \alpha_{d,wall}) \frac{\alpha_{gnd} S_g}{2} \frac{A_{d,wall}}{A_w} \\
 &= [(1 - \alpha'_{b,wall}) f_b \tan(z)' A_{b,wall} \\
 &\quad + \frac{(1 - \alpha_{d,wall})((1 - f_b) + \alpha_{gnd})}{2} A_{d,wall}] \frac{S_g}{A_w}
 \end{aligned} \tag{9}$$

301 where $\alpha'_{b,wall}$ is the “effective” albedo of the pan wall subjected to beam irra-
 302 diance, $A_{b,wall}$ [m²] is the area of the pan wall subjected to beam irradiance
 303 (=0.242 m²), $\alpha_{d,wall}$ is the albedo of the pan wall subjected to diffuse irra-
 304 diance (assumed to be a constant 0.43 (Lim et al., 2013)), α_{gnd} is the albedo
 305 of the ground surface (=0.20) and $A_{d,wall}$ [m²] is the area of the pan wall
 306 subjected to diffuse irradiance (=0.76 m²). The tangent expression converts
 307 S_b from that of a horizontal plane to that of a vertical plane. The $\tan(z)'$
 308 and $\alpha'_{b,wall}$ account for the change in solar geometry in each month over an
 309 annual cycle.

310 Over a given period (0 to τ), the estimates of $\tan(z)'$ consider the tempo-
 311 ral variation of both the sine and cosine values of the solar zenith angle (since
 312 the pan wall is on a vertical plane), i.e., $\tan(z)' = \frac{\int_0^\tau \sin(z) dt}{\int_0^\tau \cos(z) dt}$. Following that,
 313 $\tan(z)' = \frac{\sin(z)}{\cos(z)} = \tan(z)$ on an instantaneous basis; and $\tan(z)' = \frac{\overline{\sin(z)}}{\overline{\cos(z)}}$ over
 314 monthly time periods. Similar to above, we assume random transmission
 315 of the solar irradiance through the atmosphere. With the daylight period of
 316 the day divided into 1000 equal segments between sunrise and sunset (again),
 317 we estimate $\sin(z)$ and $\cos(z)$ using the solar geometry equation (given in

318 Section 2.2.1) for each segment and average over all segments for the day.
 319 We repeat this procedure for all days for the month and show the monthly
 320 average of $\tan(z)'$ in Fig. 3a. The value of $\tan(z)'$ is about 1.1 over an an-
 321 nual cycle at the equator and at least two or three times higher than that at
 322 higher latitudes and winter.

323 Similar to above (see Section 2.2.1), these contour curves resemble the
 324 ‘cosine wave’ pattern with a minimum value of about 1.01 that increase sub-
 325 stantially across the Northern and Southern hemispheres. With latitude and
 326 time of the year as part of the formulation, we again fitted an equation using
 327 the monthly average of $\tan(z)'$ in March (i.e., $M=3$ in Fig. 3a), expressed
 328 by

$$\begin{aligned}
 \tan(z)' &\approx 1.01 - [19.299 \cos^3(\phi') - 46.11 \cos^2(\phi') + 39.271 \cos(\phi') \\
 &\quad - 12.414] \\
 &= -19.299 \cos^3(\phi') + 46.11 \cos^2(\phi') - 39.271 \cos(\phi') + 13.424
 \end{aligned}
 \tag{10}$$

329 Qualitative comparison between Fig. 3a-b suggests the robustness of Eq.
 330 (10). This is confirmed by the subsequent quantitative analysis (Fig. 3c)
 331 (except winter at high latitudes).

332 Over a given period (0 to τ), the estimates of $\alpha'_{b,wall}$ consider the temporal
 333 variation of $\alpha_{b,wall}$ (Lim et al., 2013, their Appendix C.3) and the sine value
 334 of the solar zenith angle (because the pan wall is on a vertical plane), i.e.,
 335 $\alpha'_{b,wall} = \frac{\int_0^\tau \alpha_{b,wall} \sin(z) dt}{\int_0^\tau \sin(z) dt}$. On an instantaneous basis, $\alpha'_{b,wall}$ equals $\alpha_{b,wall}$
 336 because the the solar zenith angle stays the same. On a monthly basis,
 337 $\alpha'_{b,wall}$ becomes $\frac{\overline{\alpha_{b,wall} \sin(z)}}{\overline{\sin(z)}}$. Again, we divide the daylight period of the day

338 into equal segments (between sunrise and sunset) and estimate $\alpha_{b,wall} \sin(z)$
339 and $\sin(z)$ separately for each segment. We then average across segments
340 over the day and repeat this procedure for all days for the month, and show
341 monthly averages of $\alpha'_{b,wall}$ across the same range of latitudes (similar to
342 Section 2.2.1) in Fig. 4a. In short, $\alpha'_{b,wall}$ is about 0.49 at the equator and
343 declines slightly to 0.44 in winter at higher latitudes.

344 Again, these values resemble the ‘cosine wave’ pattern over an annual
345 cycle across all latitudes. With the maximum value of $\alpha'_{b,wall}$ of 0.494 that
346 decrease slightly at high latitudes, we fitted a regression curve associated
347 with the latitude and time of the year (i.e., ϕ' in Section 2.2.1) using the
348 results in March (i.e., $M=3$ in Fig. 4a), as follows

$$\begin{aligned}\alpha'_{b,wall} &\approx 0.494 - [-0.0816 \cos^2(\phi') + 0.0268 \cos(\phi') + 0.0533] \\ &= 0.0816 \cos^2(\phi') - 0.0268 \cos(\phi') + 0.4407\end{aligned}\tag{11}$$

349 The estimated results using the simplified equation here (Eq. (11); Fig. 4b)
350 well represent the spatial and temporal pattern of $\alpha'_{b,wall}$ (Fig. 4c).

351 2.2.3. Net long-wave irradiance of the pan water surface

352 The pan water surface exchanges long-wave radiation with the sky, the
353 bird guard (if any) and the rim; and the net effect may be estimated from Lim
354 et al. (2013, their Eqs. (14)-(15)). (The relative contribution of incoming
355 long-wave radiation from the atmosphere (including the bird-guard, if any)
356 and the pan wall depends on the pan geometry (i.e., height of the rim, the
357 pan diameter; see details in Appendix C).) Here, we assume that the bird
358 guard and the rim are at air temperature for simplicity. We also assume that
359 the pan water surface is at air temperature and the correction to account for

surface cooling caused by evaporation is embedded within the factor β (see Section 2). With that, the net long-wave irradiance of the pan water surface $L_{n,w}$ is approximated as

$$L_{n,w} \approx \epsilon_w \left[\left(\frac{L_i}{C} + \left(1 - \frac{1}{C} \right) \epsilon_{wall} \sigma T_a^4 \right) \frac{A_{d,w}}{A_w} + \epsilon_{wall} \sigma T_a^4 \left(1 - \frac{A_{d,w}}{A_w} \right) - \sigma T_a^4 \right] \quad (12)$$

where L_i [W m^{-2}] is the incoming long-wave irradiance of a horizontal plane, ϵ_w is the hemispherical emissivity of the pan water surface ($=0.89$), ϵ_{wall} is the hemispherical emissivity of the pan wall ($=0.82$) and σ [$\text{W m}^{-2} \text{K}^{-4}$] is the Stefan-Boltzmann constant ($=5.67 \times 10^{-8} \text{ W m}^{-2} \text{K}^{-4}$).

2.2.4. Net long-wave irradiance of the pan wall

The pan wall exchanges long-wave radiation with the sky and the surrounding ground surface, and this net effect can be estimated from Lim et al. (2013, their Eqs. (16) and (17)). We assume that the pan wall and the ground are at air temperature. Then the net long-wave irradiance of the pan wall $L_{n,wall}$ is estimated as

$$L_{n,wall} \approx \epsilon_{wall} \left[\frac{(2 - \epsilon_{gnd})L_i + \epsilon_{gnd}\sigma T_a^4}{2} - \sigma T_a^4 \right] \frac{A_{d,wall}}{A_w} \quad (13)$$

where ϵ_{gnd} is the hemispherical emissivity of the ground surface ($=0.90$).

3. Data and methods

In this study, we explicitly focus on 11 “elite” sites with complete monthly micrometeorological data (i.e., global solar irradiance (S_g), incoming long-wave irradiance (L_i), air temperature (T_a), saturated vapour pressure at

378 the same height at which air temperature is measured ($e_s(T_a)$), air vapour
379 pressure at that same height ($e_a(T_a)$) and wind speed at 2 m above ground
380 level (u_2) is available from Roderick et al. (2007) for model evaluation. These
381 sites are distributed across the Australian continent (Fig. 5). They cover
382 latitude range: -10° to -40° ; and elevation range: 0 to 600 m (Table 2).

383 We use data from existing Australian Bureau of Meteorology (BoM) dig-
384 ital records: Class A pan evaporation and wind speed (IDCJDC05.200506),
385 air temperature and humidity (IDCJHC02.200506) and radiation (NCCSOL
386 Version 2.209). The wind speed was measured using a cup anemometer at 2
387 m above ground level (i.e, u_2). The air temperature (T_a) and humidity were
388 measured in Stevenson screens.

389 Following Roderick et al. (2007), we calculated the monthly means only
390 when a minimum of 25 days was noted as validated by the BoM, and excluded
391 those months that did not meet this condition. We identified 903 months
392 (post-1995) across these sites for model evaluation (Table 2).

393 In the next section, we compare two versions of the PenPan-V2 model, i.e.,
394 the “complete” and “simplified” with the original PenPan model (Rotstayn
395 et al., 2006) and with observations. The complete version (PenPan-V2C) uses
396 the monthly averages of $A'_{b,w}$, $\alpha'_{b,w}$, $\tan(z)'$ and $\alpha'_{b,wall}$ as estimated by theory
397 (in Figs 1a, 2a, 3a and 4a, respectively). The simplified version (PenPan-
398 V2S) uses fitted regressions for those values, given by Eqs. (7), (8), (10) and
399 (11), respectively (i.e., Figs 1b, 2b, 3b and 4b, respectively).

400 4. Results

401 The spatial distribution of the 11 “elite” sites across various latitudes on
402 the Australian continent (Fig. 5) enables a site-specific examination of the
403 pan evaporation models against observations incorporating seasonal change
404 of global solar irradiance and other microclimatic conditions. The time se-
405 ries of pan evaporation observations and the comparison with the models
406 over a ten-year period (1995-2005) are shown in Fig. 6 along with estimates
407 based on the original PenPan model (Rotstayn et al., 2006). (Note that sea-
408 sonal cycles of all models are qualitatively similar, hence we only show the
409 observations and the PenPan-V2S model in the first column of Fig. 6 for
410 illustrative purposes.) In terms of the Root Mean Squared Error (RMSE)
411 and the mean absolute error (MAE), PenPan-V2C and PenPan-V2S models
412 track closely (see second and third columns of Fig. 6), implying that the
413 approximations made in the simplified version adequately represent that of
414 the complete version for all practical purposes. Both outperform the original
415 PenPan model at the majority of the study sites (8 out of 11 sites). In par-
416 ticular, results at the Broome Airport (Site: 3003; Fig. 6a), Tennant Creek
417 Airport (Site: 15135; Fig. 6e), Alice Springs Airport (Site: 15590; Fig. 6f)
418 and Cairns Aero (Site: 31011; Fig. 6h) sites demonstrate substantial im-
419 provements of the new PenPan-V2 models compared to the original PenPan
420 model. The original PenPan model gives better estimates (but statistically
421 insignificant) for the remaining 3 sites (Fig. 6d, 6j-k) in comparison with the
422 PenPan-V2 models. In terms of the slope of regression, the results show (a
423 slight) majority of the PenPan-V2 models having values closer to unity (i.e.,
424 slope equal to one) compared to the original PenPan model. Overall, the site

425 based analysis here suggests that the PenPan-V2 models better represent the
 426 variations in pan evaporation at different latitudes in comparison with the
 427 original PenPan model. (A worked example for Broome Airport (Site: 3003;
 428 December 2001) using PenPan-V2S model is given in Appendix D.)

429 To evaluate the model simulations of the seasonal cycle, we compile all
 430 data from the 11 “elite” sites and regroup those into 12 separate months.
 431 The quality indicators (RMSE, MAE, slope of regression) show that the per-
 432 formances of the PenPan-V2 models are both very similar as expected (cf.
 433 Fig. 7 and Fig. 8). Importantly, both the new formulations (Figs 7-8) clearly
 434 outperform the original PenPan model (Fig. 9). The underlying reason is the
 435 better simulation of the seasonal radiation components ($A'_{b,w}$, $\alpha'_{b,w}$, $\tan(z)'$
 436 and $\alpha'_{b,wall}$) that all depend on solar geometry. Whilst the formulation struc-
 437 ture of MAE does not magnify large errors as much as that of the RMSE,
 438 in a seasonal cycle, it shows a high in summer (December/January) and a
 439 low in winter (June/July) for all models. This might imply the limitation of
 440 the monthly mean meteorological measurements without covariance to fully
 441 characterise the diurnal variation of driving forces of pan evaporation (see
 442 Lim and Roderick (2014)). Nonetheless, the advantage of the new formu-
 443 lation here over the original PenPan model in the seasonal pan evaporation
 444 simulation remains intact.

445 To generalise the global performance of these models, we combined the
 446 above results and show the outcomes of radiative component ($E_{pan,R}$), aero-
 447 dynamic component ($E_{pan,A}$) and their sum (E_{pan}) for each model (Fig. 10).
 448 The estimated $E_{pan,R}$ values of the PenPan-V2 models are slightly lower than
 449 that of the original PenPan model, but balanced by slightly higher estimated

450 $E_{pan,A}$ values of the PenPan-V2 models relative to the original PenPan model.
 451 Consistent with our findings above (Figs 6-9), the global analysis here con-
 452 firms the estimated E_{pan} values of the PenPan-V2 models are generally more
 453 accurate (RMSE = 18.3 mm mth⁻¹, MAE = 13.9 mm mth⁻¹) than that of
 454 the original PenPan model (RMSE = 21.5 mm mth⁻¹, MAE = 16.4 mm
 455 mth⁻¹). Transforming our understanding of the non-steady state physics of
 456 pan evaporation (Lim et al., 2012, 2013) to the new steady state formula-
 457 tion has improved the overall accuracy by ~ 3 mm mth⁻¹ (i.e., ~ 3 W m⁻² in
 458 energetic terms) relative to the original PenPan model.

459 To understand the underlying physics, we show the pan evaporation con-
 460 tributed by net short-wave irradiance ($\frac{S_n}{\lambda\rho_w}$), net long-wave irradiance ($\frac{L_n}{\lambda\rho_w}$)
 461 and the net irradiance ($\frac{R_n}{\lambda\rho_w}$) of each of the models (Fig. 11). The estimated
 462 $\frac{S_n}{\lambda\rho_w}$ values of the PenPan-V2 models are lower than that of the original Pen-
 463 Pan model (top panel of Fig. 11a-c). These results reflect the rigorous formu-
 464 lation for the short-wave irradiance of the pan water surface and the pan wall
 465 of the PenPan-V2 models in contrast with the original PenPan model. The
 466 estimated $\frac{L_n}{\lambda\rho_w}$ values of the PenPan-V2 models are larger (in absolute sense)
 467 than that of the original PenPan model (middle panel of Fig. 11a-c) because
 468 they also account for the net loss of the long-wave irradiance from the pan
 469 wall to the surroundings (i.e., the sky and the ground surface). Following the
 470 basic formulation in Section 2 (Eqs. (1)-(2)), the results of estimated $\frac{R_n}{\lambda\rho_w}$
 471 versus observed pan evaporation (bottom panel of Fig. 11a-c) distributed
 472 above (below) the 1:1 line can be understood as the estimated E_{pan} values
 473 are achieved by energy balance through losing (absorbing) the net sensible
 474 heat into (from) the air. The estimated $\frac{R_n}{\lambda\rho_w}$ values of the PenPan-V2 models

475 peak at $\sim 300 \text{ mm mth}^{-1}$ (bottom panel of Fig. 11a-b). Within this range,
 476 the PenPan-V2 models have more tendency to absorb sensible heat from the
 477 air than the original PenPan model, and this is consistent with the general
 478 understanding of the consequence of evaporative cooling (Lim et al., 2013).
 479 When the observed E_{pan} exceeds 300 mm mth^{-1} , the excess pan evaporation
 480 is driven by net absorption of sensible heat. For the radiative part of the
 481 combination equation, the general pattern of $\frac{R_n}{\lambda \rho_w}$ and the peak (i.e., ~ 300
 482 mm mth^{-1}) is in good agreement with that revealed by our experimental pan
 483 (Lim et al., 2013, their Fig. 9b). Thus both the PenPan-V2C and PenPan-
 484 V2S models are equally reliable over the range studied here. In contrast,
 485 the estimated $\frac{R_n}{\lambda \rho_w}$ values of the original PenPan model could reach as high
 486 as 400 mm mth^{-1} , exceeding that of our experimental pan by $\sim 100 \text{ W m}^{-2}$
 487 (or 100 mm mth^{-1}). In addition, the original PenPan model is inclined to
 488 over-estimate the contribution of the net irradiance towards pan evaporation.
 489 This is mainly because of the relatively simplified radiative formulation of
 490 the original PenPan model (see Section 1, points (ii)-(iv)), particularly for
 491 the constant albedo of the pan.

492 The new formulation presented here is based on the first-order Taylor
 493 approximation of the saturated vapour pressure (Appendix A) and a fur-
 494 ther approximation made in the net long-wave irradiance of the pan wa-
 495 ter surface (Section 2.2.3). This invites consideration of potential improve-
 496 ment in model accuracy by introducing non-linear energy balance equa-
 497 tions (Paw U and Gao, 1988; Milly, 1991; Baldocchi et al., 2005). With
 498 that in mind, we re-formulated Eq. (1) to account for a second-order Tay-
 499 lor series approximation of the saturation vapour pressure (i.e., $e_s(T_s) \approx$

500 $e_s(T_a) + s(T_s - T_a) + \frac{1}{2} \frac{ds}{dT_a} (T_s - T_a)^2$ and/or the linearised version of emission
 501 of long-wave radiation at the pan water surface (i.e., $T_s^4 \approx T_a^4 + 4T_a^3(T_s - T_a)$).
 502 Despite the added complexities (e.g., solving of lengthy quadratic equations),
 503 we found that model accuracy using these non-linear equations are, at best,
 504 on a par with the PenPan-V2 models. Whilst re-formulation using much
 505 higher-order Taylor series approximations are possible, the practical signifi-
 506 cance remains questionable (Paw U and Gao, 1988; Milly, 1991). The fun-
 507 damental structure of Penman’s combination equation is to eliminate the
 508 surface temperature in favour of using the (observed) air temperature and
 509 a (linear) expansion around the air temperature. It is important to under-
 510 stand that this approach allows errors to at least partly cancel. For example,
 511 assume the surface temperature was substantially colder than the air tem-
 512 perature. By using a mass transfer approach with the observed air tempera-
 513 ture, we would over-estimate the aerodynamic component but we would also
 514 under-estimate the radiative component and any error (from assuming the
 515 pan water surface temperature equals the air temperature) would at least
 516 partly cancel in the combination equation. That might explain why we did
 517 not see any benefit of adding higher-order terms to the Penman approxima-
 518 tion.

519 **5. Discussion and summary**

520 The aerodynamic function used here (Eq. (4)) is based on our ealier work
 521 (Lim et al., 2012) and was found appropriate for long-term (e.g., monthly)
 522 applications (Lim and Roderick, 2014, their Fig. 5). The subsequent ap-
 523 proximation is based on several physical variables (wind speed at 2 m above

ground level u_2 , atmospheric pressure P_a and a dimensionless number that scales u_2 to the pan water surface, n ; Eq. (3)) in contrast with the typical “wind function” (i.e., $f(u) = a + bu$). We assigned the dimensionless number (n) to account for the bird guard effect (if any) for the pan. Therefore the aerodynamic function used here should provide adequate physical representation of the aerodynamic component of pan evaporation ($E_{pan,A}$). It is also possible to test its applicability across a wider set of climate conditions, such as pans at high elevation (Blaney, 1960; Giambelluca and Nullet, 1992).

The formulation of the net irradiance of the pan presented here (Section 2.2) is an approximation of our earlier works using a highly instrumented US Class A pan (Lim et al., 2013). It addresses the geometry of the system (the pan diameter, the height of the water level, the height of the rim and the solar zenith angle), albedos and emissivities of the pan water surface and the pan wall. For the short-wave irradiance, several components of the new PenPan-V2 models ($A'_{b,w}$, $\alpha'_{b,w}$, $\tan(z)'$, $\alpha'_{b,wall}$) vary with solar geometry and can be estimated by theoretical and regression approaches (Figs 1-4, respectively). The comparisons here show that the new PenPan-V2 models outperform the original PenPan model across different latitudes but especially across different seasons. For the long-wave irradiance, the level of detail represented in our formulation for both the pan water surface and the pan wall (Eq. (12)-(13)) is an extension of that in the original PenPan model. Incorporation of the correction factor to account for the shading effect of the bird guard (C) provides better physical interpretation on the radiative exchange of the pan. Following this, the steady state formulation here improves the calculation of heat transfer at the pan water surface and the pan wall (see

Appendix D) compared to the existing literature (e.g., Linacre (1994); Rotstayn et al. (2006); McVicar et al. (2007)). We also note that the formulation here assumes a random distribution of clouds within the day and over the month. When short-term (i.e., sub-daily) measurements are available, up-scaling such short-term process-level understanding over time periods long enough to reach a steady state (i.e., monthly) should further improve the model accuracy.

The PenPan-V2S model remains relatively simple but better represents observations of monthly pan evaporation. It would be interesting to see how it compares against a large network of pan evaporation observations available elsewhere (i.e., latitude ranges -60° to 60°). The new model should be useful for understanding climate change such as terrestrial water availability using large networks of evaporation pans (e.g., McVicar et al. (2012); Roderick et al. (2007, 2009a,b); Shuttleworth et al. (2009)). It should also be helpful for evaluating the outputs of GCMs (e.g., Rotstayn et al. (2006)) and hence the assessment of terrestrial water availability under various future climate scenarios (e.g., Johnson and Sharma (2010)).

Appendices

Appendix A. Derivation of open water surface evaporation

Here, we show the derivation of open water surface evaporation based on the combination of mass and energy balance method (Penman, 1948) associated with the boundary layer concept for heat and mass transfer (Lim et al., 2012, 2013). The energy balance equation for an open water surface evaporation is expressed as

$$\lambda \rho_w E_{ow} = (R_n - \Delta Q) - H_n \quad (\text{A.1})$$

where λ [J kg⁻¹] is the latent heat of vaporisation of liquid water (~ 2.45 MJ kg⁻¹), ρ_w [kg m⁻³] is the density of liquid water (≈ 1000 kg m⁻³), E_{ow} [m s⁻¹] is the evaporation rate of the open water surface, R_n [W m⁻²] is the net irradiance of the water body, ΔQ [W m⁻²] is the increase in the heat storage of the water body and H_n [W m⁻²] is the net sensible heat loss of the water body. The equation to estimate λ is given in Appendix B.

Following Lim et al. (2012), we formulate the open water surface evaporation as

$$E_{ow} = \frac{M_w}{R \rho_w} \frac{D_v}{T_a} \frac{1}{\Delta z_{ow}} (e_s(T_s) - e_a(T_a)) \quad (\text{A.2})$$

where $e_s(T_s)$ [Pa] is the vapour pressure at the evaporating surface, $e_a(T_a)$ [Pa] is the air vapour pressure at the same height at which air temperature (T_a , [K]) is measured, M_w [kg mol⁻¹] is the molecular mass of water ($= 0.018$ kg mol⁻¹), R [J mol⁻¹ K⁻¹] is the ideal gas constant ($= 8.314$ J mol⁻¹ K⁻¹), D_v [m² s⁻¹] is the diffusion coefficient for water vapour in air and Δz_{ow} [m] is the boundary layer thickness of the open water surface. (Note that Δz_{ow} can be parameterised following Lim et al. (2012, their Eq. (15)). We do not do it here because it is beyond the scope of this manuscript.)

The vapour pressure at the evaporating surface can be formulated using the Penman approximation (see Monteith and Unsworth (2008)), i.e.,

$$e_s(T_s) \approx e_s(T_a) + s (T_s - T_a) \quad (\text{A.3})$$

591 where $e_s(T_a)$ [Pa] is saturated vapour pressure at the same height at which
 592 T_a is measured and s [Pa K⁻¹] is the slope of the saturation vapour pressure
 593 versus temperature curve at air temperature (T_a) and T_s [K] is the evaporat-
 594 ing surface temperature. The equation to estimate s is given in Appendix
 595 B.

596 We express the net sensible heat loss of the water body as

$$H_n = \frac{k_a}{\Delta z_{ow}}(T_s - T_a) \quad (\text{A.4})$$

597 where k_a [W m⁻¹ K⁻¹] is the thermal conductivity of air. Note that $k_a =$
 598 $D_h \rho_a C_p$ (Monteith and Unsworth, 2008), where D_h [m² s⁻¹] is the thermal
 599 diffusivity of air, ρ_a [kg m⁻³] is the density of air and C_p [J kg⁻¹] is the heat
 600 capacity of dry air. (We provide the equations to estimate k_a and D_h in
 601 Appendix B.) With that, Eq. (A.4) becomes

$$H_n = \frac{D_h \rho_a C_p}{\Delta z_{ow}}(T_s - T_a) \quad (\text{A.5})$$

602 Based on the ideal gas law, we assume that the density of air approximates
 603 that of dry air. Hence $\rho_a \approx \frac{P_a M_a}{R T_a}$, where P_a [Pa] is the atmospheric pressure
 604 and M_a [kg mol⁻¹] is the molecular mass of air (=0.029 kg mol⁻¹). By
 605 rearranging the formulation of the psychrometric constant ($\gamma = \frac{C_p P_a}{\frac{M_w}{M_a} \lambda}$, [Pa
 606 K⁻¹], ~ 67 Pa K⁻¹), we have $C_p = \frac{M_w \lambda \gamma}{M_a P_a}$ (Monteith and Unsworth, 2008).
 607 Substituting these equations (i.e., ρ_a , C_p) into Eq. (A.4), we re-write Eq.
 608 (A.5) as

$$H_n = \lambda \gamma \frac{M_w}{R} \frac{D_h}{T_a} \frac{1}{\Delta z_{ow}}(T_s - T_a) \quad (\text{A.6})$$

By substituting Eqs. (A.2), (A.3) and (A.6) into Eq. (A.1) and after rearrangement, we have

$$T_s - T_a = - \frac{\lambda \frac{M_w}{R} \frac{D_v}{T_a} \frac{1}{\Delta z_{ow}} (e_s(T_a) - e_a(T_a)) - (R_n - \Delta Q)}{\lambda \frac{M_w}{R} \frac{1}{T_a} \frac{1}{\Delta z_{ow}} (D_v s + D_h \gamma)} \quad (\text{A.7})$$

By substituting Eqs. (A.6) and (A.7) into Eq. (A.1), we eliminate the water surface temperature (T_s) and formulate the open water surface evaporation as

$$\begin{aligned} E_{ow} &= \frac{(R_n - \Delta Q)}{\lambda \rho_w} + \frac{\frac{D_h}{D_v} \gamma}{s + \frac{D_h}{D_v} \gamma} \left[\frac{M_w}{R \rho_w} \frac{D_v}{T_a} \frac{1}{\Delta z_{ow}} (e_s(T_a) - e_a(T_a)) \right. \\ &\quad \left. - \frac{(R_n - \Delta Q)}{\lambda \rho_w} \right] \\ &= \frac{(R_n - \Delta Q)}{\lambda \rho_w} + \frac{\beta_{ow} \gamma}{s + \beta_{ow} \gamma} \left[f_{v,ow} (e_s(T_a) - e_a(T_a)) - \frac{(R_n - \Delta Q)}{\lambda \rho_w} \right] \\ &= \frac{s}{s + \beta_{ow} \gamma} \frac{(R_n - \Delta Q)}{\lambda \rho_w} + \frac{\beta_{ow} \gamma}{s + \beta_{ow} \gamma} [f_{v,ow} (e_s(T_a) - e_a(T_a))] \end{aligned} \quad (\text{A.8})$$

where $f_{v,ow}$ [$\text{m s}^{-1} \text{Pa}^{-1}$] is the aerodynamic function of the open water surface ($= \frac{M_w}{R \rho_w} \frac{D_v}{T_a} \frac{1}{\Delta z_{ow}}$) and β_{ow} is the ratio of heat to mass transfer coefficients for the open water surface ($= \frac{D_h}{D_v}$). For the typical range of air temperature ($273.15 \text{ K} \leq T_a \leq 313.15 \text{ K}$) and elevation (range: 0 to 1000 m), we estimate that β_{ow} varies from ~ 0.85 to ~ 0.88 . For all practical purposes, we assume $\beta_{ow} \approx 0.87$ and approximate Eq. (A.7) under steady state conditions (i.e., $\Delta Q \approx 0$) as

$$E_{ow} \approx \frac{s}{s + 0.87 \gamma} \frac{R_n}{\lambda \rho_w} + \frac{0.87 \gamma}{s + 0.87 \gamma} [f_{v,ow} (e_s(T_a) - e_a(T_a))] \quad (\text{A.9})$$

621 Here β_{ow} is simply calculated as the ratio of thermal diffusivity of air to
622 diffusion coefficient for water vapour in air (i.e., $\frac{D_h}{D_v} \approx 0.87$) because the
623 surface areas for both heat and mass transfer are identical. For water bodies
624 / containers with additional surface areas for heat transfer (e.g., a US Class
625 A pan or chinese micro-pan), this value would be higher.

626 The derivation presented here (i.e., Eq. (A.9)) is different from that of
627 lake evaporation in Penman (1948). The latter implicitly assumes that the
628 thermal diffusivity of air (D_h) and the diffusion coefficient for water vapour
629 in air (D_v) are equal, and hence the factor 0.87 is missing in the original
630 formulation by Penman (1948).

631 **Appendix B. Miscellaneous equations**

632 In this section, we list the equations for calculating the latent heat of
633 vaporisation of liquid water λ [J kg⁻¹], slope of the saturation vapour pres-
634 sure versus temperature curve at air temperature s [Pa K⁻¹], psychrometric
635 constant γ [Pa K⁻¹], atmospheric pressure P_a [Pa], beam fraction f_b [dimen-
636 sionless], thermal conductivity of air k_a [W m⁻¹ K⁻¹], thermal diffusivity of
637 air D_h [m² s⁻¹] and diffusion coefficient for water vapour in air D_v [m² s⁻¹]
638 in Table B.1.

639 **Appendix C. Boundary conditions of the pan**

640 Following Lim et al. (2013), the formulation here assumes a partially
641 filled pan with water level ~ 0.2 m for an operational US Class A pan. Apart
642 from blocking of the shortwave irradiance (see the first paragraph in Section
643 2.2.1), we formulated a mathematical equation to quantify the pan water

644 surface area subjected to diffuse irradiance ($A_{d,w}$) as a fraction of the pan
 645 water surface area (A_w) for a partially filled pan by integration (Lim et al.,
 646 2013, their Eq. (B.2)). It takes into account the pan geometry, e.g., height of
 647 the rim (h_e) and the pan diameter (D) (Fig. C.1). It involves the sum of the
 648 two separate fractions (θ_1/π , θ_1/π), which vary with the distance from the
 649 edge of the pan water surface (x). With this equation, we found that for $D =$
 650 1.21 m and $h_e = 0.055$ m, we get $A_{d,w} = 0.88 A_w$. This means that 88% of the
 651 pan water surface receives incoming diffuse (short- and long-wave) irradiance
 652 from the atmosphere. The remaining 12% of the pan water surface receives
 653 incoming long-wave irradiance from the pan wall.

654 Lim et al. (2012, their Section 5) evaluated the contribution of rim as part
 655 of system in the energy balance of the pan and did not find its significance.
 656 This is probably because the heat transfer between the rim and the bulk
 657 water is small. Following that, we exclude radiative interception at the rim
 658 of the pan and assume the temperature of the rim equals the air temperature
 659 in our formulation. (For a Chinese micro-pan with diameter of 0.2 m (Fu et
 660 al. , 2004), the contribution of rim to the energy balance of the pan remains
 661 a subject for further experimental investigation.)

662 **Appendix D. Worked example**

663 To assist readers in better understanding the steps involved in the PenPan-
 664 V2S model, we prepared a worked example using observations for a single
 665 month at Broome Airport (Site: 3003; December 2001) (see Fig. 6a). The
 666 inputs (including the calculated value of radiation arriving at the top of at-
 667 mosphere on 15th December using Roderick (1999, Appendix A)) are listed

⁶⁶⁸ in Table D.1. The outputs of the calculations are given in Table D.2.

669 **Acknowledgement**

670 We acknowledge the Australian Research Council (ARC) for the financial
671 support of this study through the grants DP0879763 and CE11E0098. WHL
672 also acknowledge the Oxford Martin School for the financial support through
673 the OMPORS grant. We are grateful to Tim R. McVicar and two anonymous
674 reviewers for helpful comments.

675 **References**

- 676 Allen, R. G., Pereira, L. S., Raes, D., Smith, M., 1998. Crop evapotranspira-
677 tion - Guidelines for computing crop water requirements. FAO Irrigation
678 and Drainage Paper 56. FAO, Rome.
- 679 Baldocchi, D. D., Krebs, T., Leclerc, M. Y., 2005. “Wet/dry Daisyworld”: a
680 conceptual tool for quantifying the spatial scaling of heterogeneous land-
681 scapes and its impact on the subgrid variability of energy fluxes. *Tellus*
682 57B, 175-188, doi: 10.3402/tellusb.v57i3.16538.
- 683 Blaney, H. F., 1960. Evaporation from water surfaces in mountain
684 areas of western United States. *Hydrol. Sci. J.* 5, 27-37, doi:
685 10.1080/02626666009493161.
- 686 Brutsaert, W., Parlange, M. B., 1998. Hydrologic cycle explains the evapo-
687 ration paradox. *Nature* 396, 30-30, doi: 10.1038/23845.
- 688 Chu, C.R., Li, M.H., Chen, Y.Y., Kuo, Y.H., 2010. A wind tunnel experiment
689 on the evaporation rate of Class A evaporation pan. *J. Hydrol.* 381, 221-
690 224, doi: 10.1016/j.jhydrol.2009.11.044.

- 691 Fu, G., Liu, C., Chen, S., Hong, J., 2004. Investigating the conversion co-
692 efficients for free water surface evaporation of different evaporation pans.
693 Hydrol. Processes 18, 2247-2262, doi: 10.1002/hyp.5526.
- 694 Giambelluca, T. W., Nullet, D., 1992. Evaporation at high elevations in
695 Hawaii. J. Hydrol. 136, 219-235, doi: 10.1016/0022-1694(92)90012-K.
- 696 Giblett, M.A., 1921. Some problems connected with evaporation from large
697 expanses of water. Proc. R. Soc. London, Ser. A 99, 472-490.
- 698 Jones, H. G., 1976. Crop characteristics and the ratio between assimilation
699 and transpiration. J. Appl. Ecol. 13, 605-622, doi: 10.2307/2401807.
- 700 Liebert, C.H., 1965. Spectral emittance of aluminum oxide and zinc oxide on
701 opaque substrates. NASA Tech. Note, TN D-3115. NASA, Washington,
702 D.C.
- 703 Jacobson, M. Z., 2005. Fundamentals of Atmospheric Modeling, 2nd ed.
704 Cambridge University Press, New York.
- 705 Johnson, F., Sharma, A., 2010. A comparison of Australian open water body
706 evaporation trends for current and future climates estimated from class
707 A evaporation pans and general circulation models. J. Hydrometeorol. 11,
708 105-121, doi: 10.1175/2009jhm1158.1.
- 709 Kohler, M. A., Noredenson, T. J., Fox, W. E., 1955. Evaporation from pans
710 and lakes. US Weather Bureau Research Paper 38. US Weather Bureau,
711 Washington, D.C.

712 Lim, W. H., Roderick, M. L., Hobbins, M. T., Wong, S. C., Groeneveld, P.
713 J., Sun, F., Farquhar, G. D., 2012. The aerodynamics of pan evaporation.
714 Agric. For. Meteorol. 152, 31-43, doi: 10.1016/j.agrformet.2011.08.006.

715 Lim, W. H., Roderick, M. L., Hobbins, M. T., Wong, S. C., Farquhar, G.
716 D., 2013. The energy balance of a US Class A evaporation pan, Agric. For.
717 Meteorol. 182-183, 314-331, doi: 10.1016/j.agrformet.2013.07.001.

718 Lim, W. H., Roderick, M. L., 2014. Up-scaling short-term process-level un-
719 derstanding to longer timescales using a covariance-based approach. Hy-
720 drol. Earth Syst. Sci. 18, 31-45, doi: 10.5194/hess-18-31-2014.

721 Linacre, E. T., 1994. Estimating U.S. Class A pan evaporation from few
722 climate data. Water Int. 19, 5-14, doi: 10.1080/02508069408686189.

723 McVicar, T. R., Roderick, M. L., Donohue, R. J., Li, L. T., Van Niel, T.
724 G., Thomas, A., Grieser, J., Jhajharia, D., Himri, Y., Mahowald, N. M.,
725 Mescherskaya, A. V., Kruger, A. C., Rehman, S., Dinpashoh, Y., 2012.
726 Global review and synthesis of trends in observed terrestrial near-surface
727 wind speeds: Implications for evaporation, J. Hydrol. 416, 182-205, doi:
728 10.1016/j.jhydrol.2011.10.024.

729 McVicar, T. R., Van Niel, T. G., Li, L. T., Hutchinson, M. F., Mu, X. M., Liu,
730 Z. H., 2007. Spatially distributing monthly reference evapotranspiration
731 and pan evaporation considering topographic influences, J. Hydrol. 338,
732 196-220, doi: 10.1016/j.jhydrol.2007.02.018.

733 Milly, P.C.D, 1991. A refinement of the combination equations for evapora-
734 tion. Surv. Geophys. 12, 145-154. doi: 10.1007/BF01903416.

- 735 Monteith, J. L., Unsworth, M. H., 2008. Principles of Environmental Physics,
736 3rd ed. Elsevier Academic Press, San Diego.
- 737 Ohmura, A., Wild, M., 2002. Is the hydrological cycle accelerating? Science
738 298, 1345-1346, doi: 10.1126/science.1078972.
- 739 Paw U, K. T., Gao, W., 1988. Applications of solutions to non-linear energy
740 budget equations. Agric. For. Meteorol. 43, 121-145, doi: 10.1016/0168-
741 1923(88)90087-1.
- 742 Peisker, M., 1973. CO₂-aufnahme, transpiration und blatttemperatur unter
743 dem Einfluß von Änderungen der stomataweite. Die Kulturpflanze 21, 97-
744 109, doi: 10.1007/bf02103157.
- 745 Penman, H. L., 1948. Natural evaporation from open water, bare soil and
746 grass. Proc. R. Soc. London, Ser. A 193, 120-145.
- 747 Peterson, T. C., Golubev, V. S., Groisman, P. Y., 1995. Evaporation losing
748 its strength. Nature 377, 687-688, doi: 10.1038/377687b0.
- 749 Pruppacher, H.R. and Klett, J.D., 1997. Microphysics of Clouds and Pre-
750 cipitation, second rev. & enl. ed. Kluwer Academic Publishers, Dordrecht,
751 Netherlands.
- 752 Roderick, M. L., 1999. Estimating the diffuse component from daily and
753 monthly measurements of global radiation. Agric. For. Meteorol. 95, 169-
754 185, doi: 10.1016/S0168-1923(99)00028-3.
- 755 Roderick, M. L., Farquhar, G. D., 2002. The cause of decreased pan

756 evaporation over the past 50 years. *Science* 298, 1410-1411, doi:
757 10.1126/science.1075390-a.

758 Roderick, M. L., Hobbins, M. T., Farquhar, G. D., 2009a. Pan evaporation
759 trends and the terrestrial water balance. I. Principles and observations.
760 *Geogr. Compass* 3, 746-760, doi: 10.1111/j.1749-8198.2008.00213.x.

761 Roderick, M. L., Hobbins, M. T., Farquhar, G. D., 2009b. Pan evaporation
762 trends and the terrestrial water balance. II. Energy balance and interpreta-
763 tion. *Geogr. Compass* 3, 761-780, doi: 10.1111/j.1749-8198.2008.00214.x.

764 Roderick, M. L., Rotstayn, L. D., Farquhar, G. D., Hobbins, M. T., 2007.
765 On the attribution of changing pan evaporation. *Geophys. Res. Lett.* 34,
766 L17403, doi: 10.1029/2007GL031166.

767 Rotstayn, L. D., Roderick, M. L., Farquhar, G. D., 2006. A simple pan-
768 evaporation model for analysis of climate simulations: Evaluation over
769 Australia. *Geophys. Res. Lett.* 33, L17715, doi: 10.1029/2006GL027114.

770 Shuttleworth, W. J., Serrat-Capdevila, A., Roderick, M. L., Scott, R. L.,
771 2009. On the theory relating changes in area-average and pan evaporation.
772 *Q. J. R. Meteorol. Soc.* 135, 1230-1247, doi: 10.1002/qj.434.

773 Stanhill, G., 2002. Is the Class A evaporation pan still the most practi-
774 cal and accurate meteorological method for determining irrigation water
775 requirements? *Agric. Forest Meteorol.* 112, 233-236, doi: 10.1016/S0168-
776 1923(02)00132-6.

777 Thom, A. S., Thony, J. L., Vauclin, M., 1981. On the proper employment

778 of evaporation pans and atmometers in estimating potential transpiration.
779 Quart. J. R. Meteorol. Soc. 107, 711-736, doi: 10.1002/qj.49710745316.

780 van Dijk, M. H., 1985. Reduction in evaporation due to the bird screen used
781 in the Australian class A pan evaporation network. Aust. Meteorol. Mag.
782 33, 181-183.

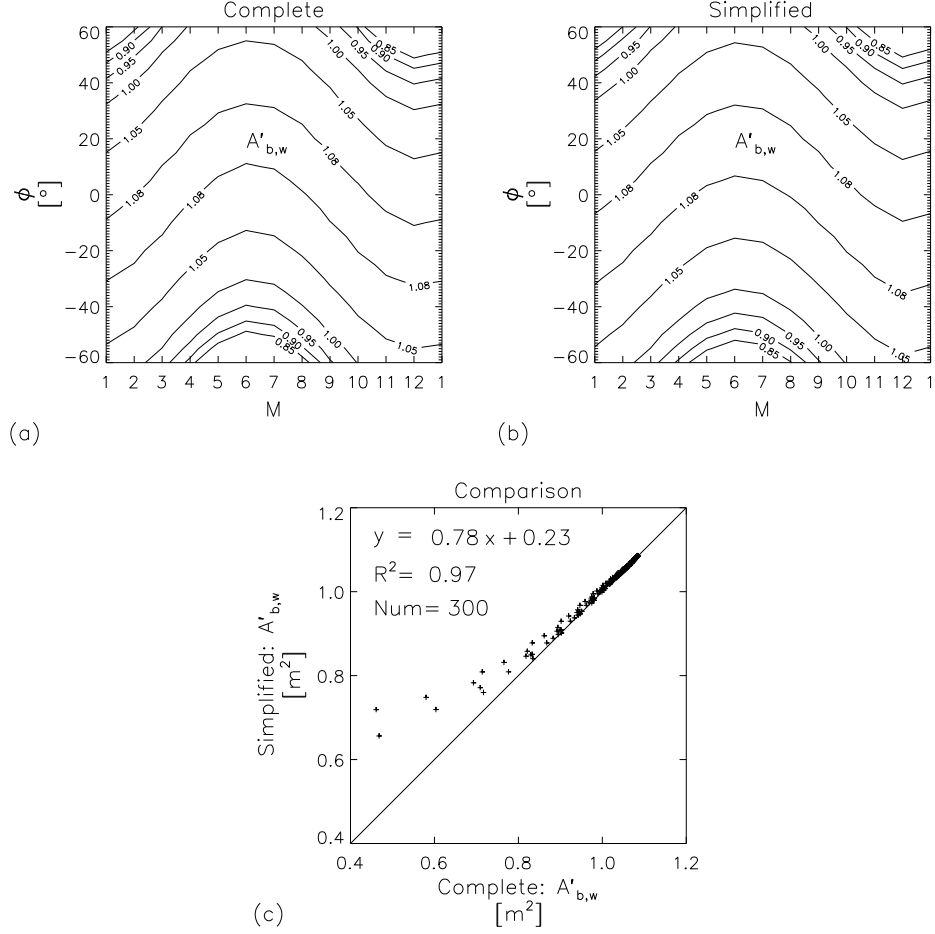


Fig. 1: The impact of shade cast by the rim changing the “effective” area of pan water surface subjected to beam irradiance $A'_{b,w}$ with respect to the latitude (ϕ ; positive and negative signs mean Northern and Southern hemispheres, respectively) and the middle of each month (M): (a) Complete, (b) Simplified using Eq. (11), (c) Comparison between (a) and (b).

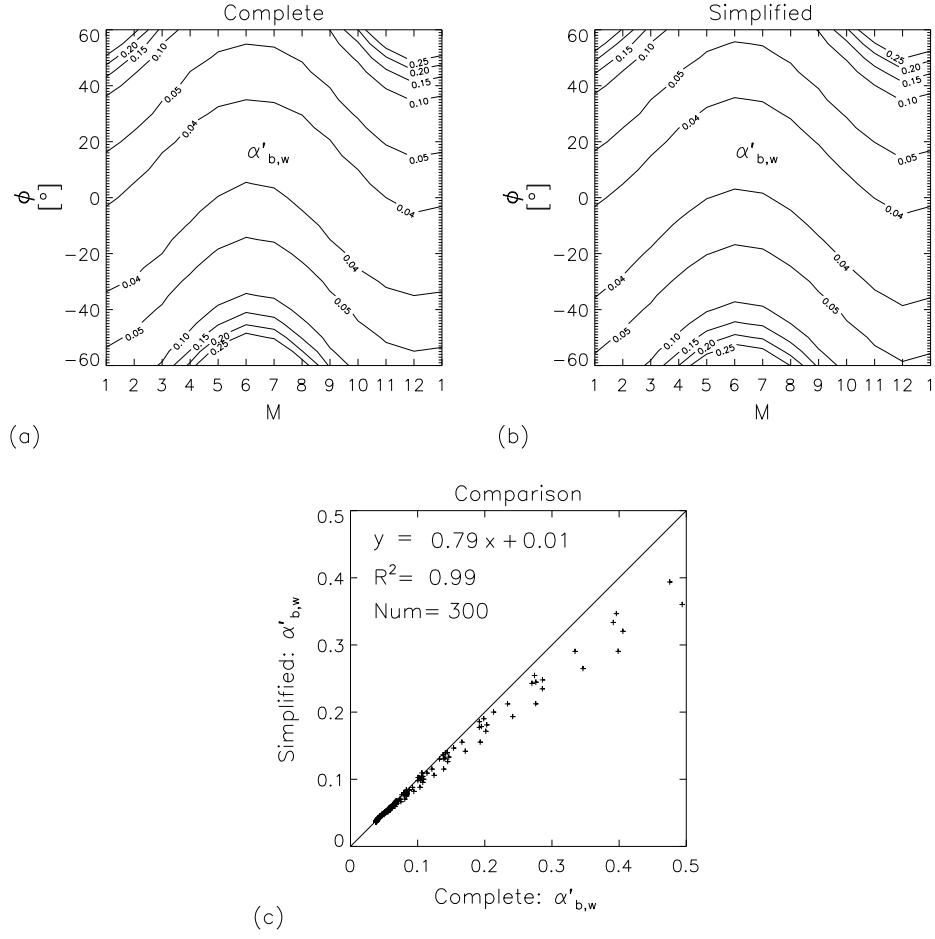


Fig. 2: The change of “effective” albedo of pan water surface subjected to beam irradiance $\alpha'_{b,w}$ with respect to the latitude (ϕ ; positive and negative signs mean Northern and Southern hemispheres, respectively) and the middle of each month (M): (a) Complete, (b) Simplified using Eq. (11), (c) Comparison between (a) and (b).

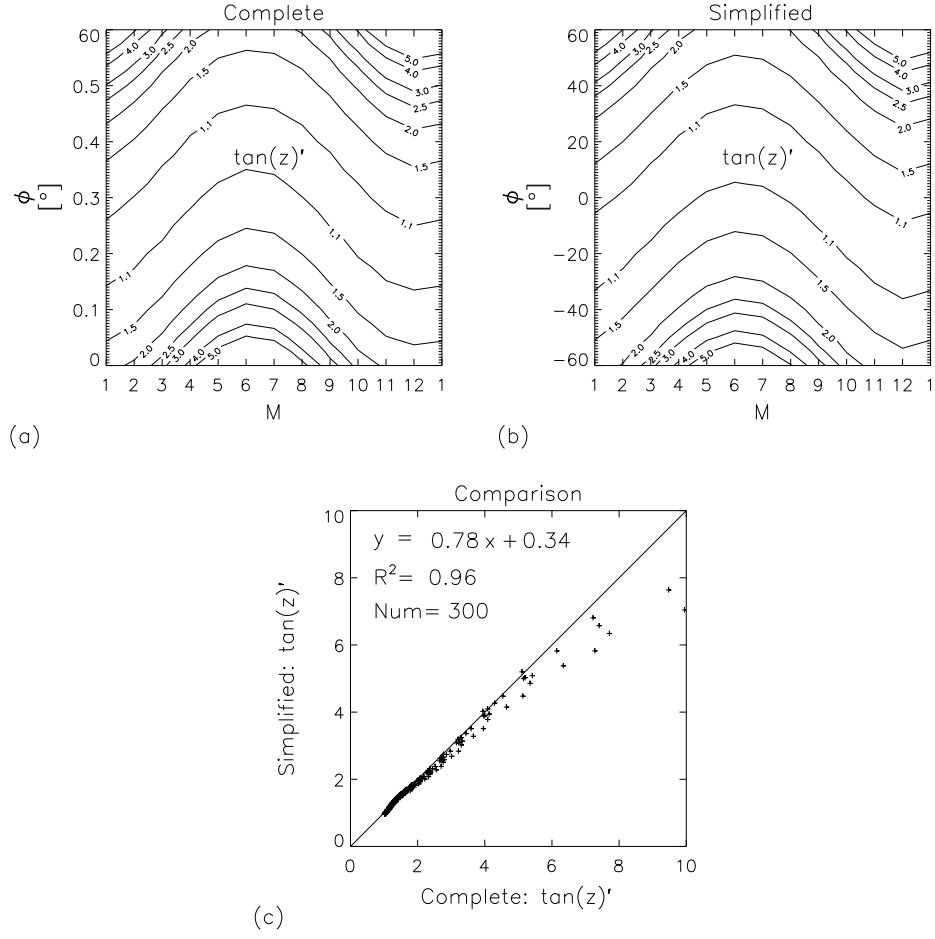


Fig. 3: The change of “effective” tangential value of solar zenith angle $\tan(z)'$ with respect to the latitude (ϕ ; positive and negative signs mean Northern and Southern hemispheres, respectively) and the middle of each month (M): (a) Complete, (b) Simplified using Eq. (11), (c) Comparison between (a) and (b).

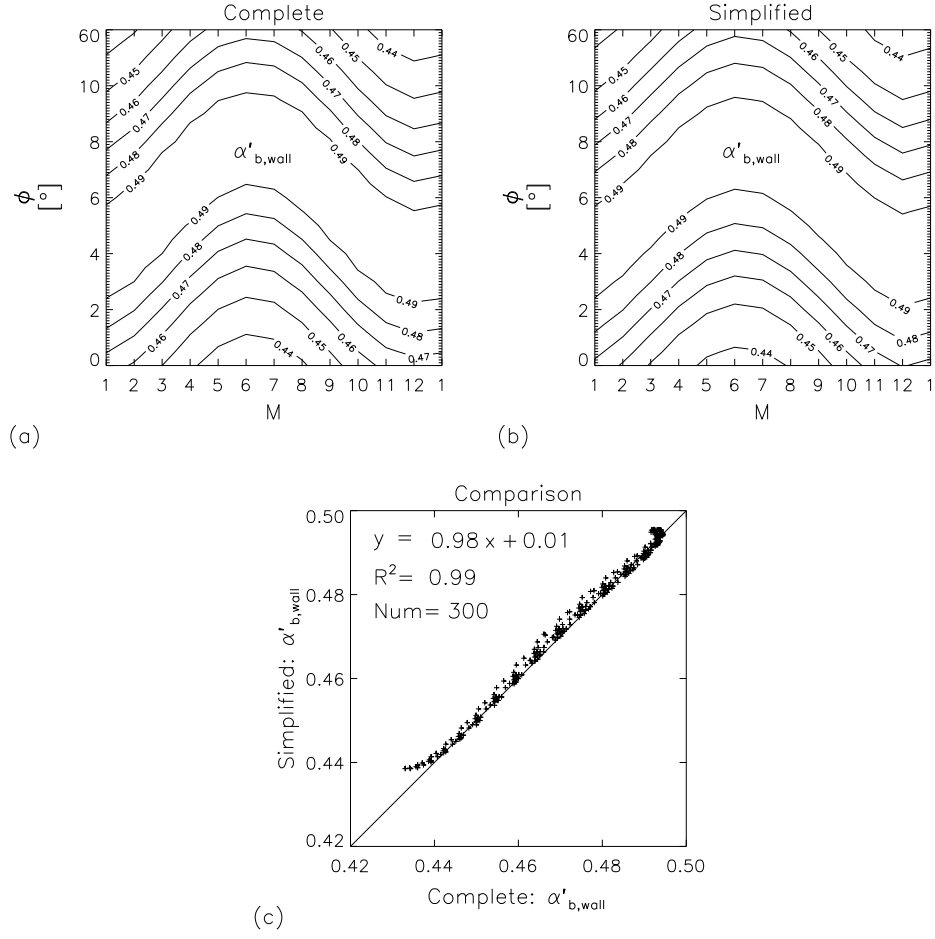


Fig. 4: The change of “effective” albedo of pan wall subjected to beam irradiance $\alpha'_{b,wall}$ with respect to the latitude (ϕ ; positive and negative signs mean Northern and Southern hemispheres, respectively) and the middle of each month (M): (a) Complete, (b) Simplified using Eq. (11), (c) Comparison between (a) and (b).

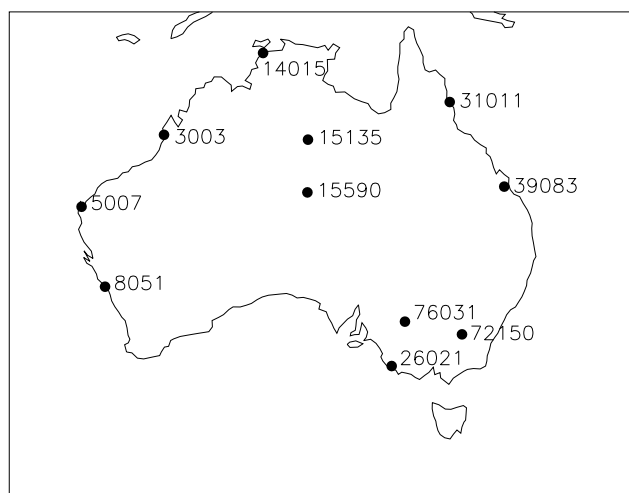


Fig. 5: The locations of 11 “elite” sites (listed in Table 2) in Australia.

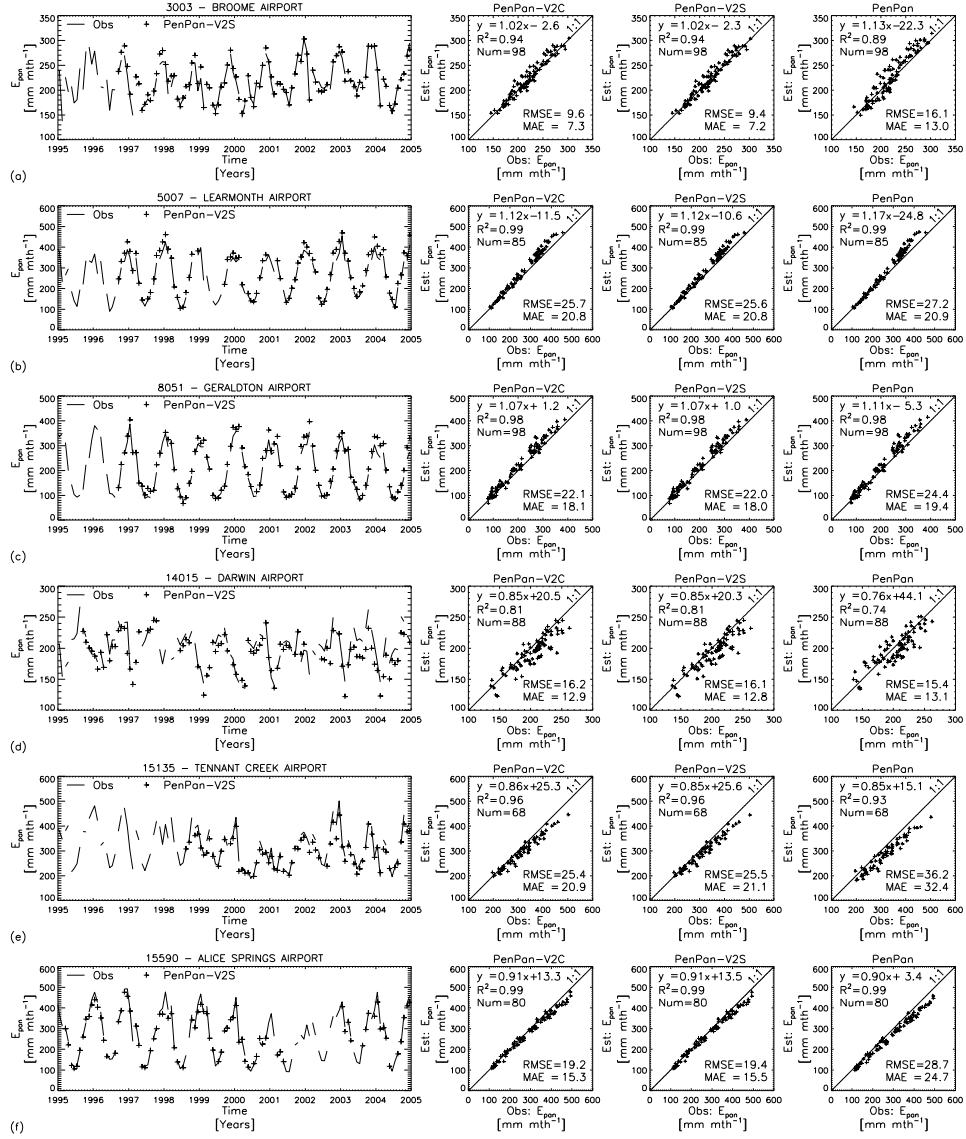


Fig. 6: Comparing estimated E_{pan} (PenPan-V2C, PenPan-V2S and PenPan models) with observations at 11 "elite" sites.

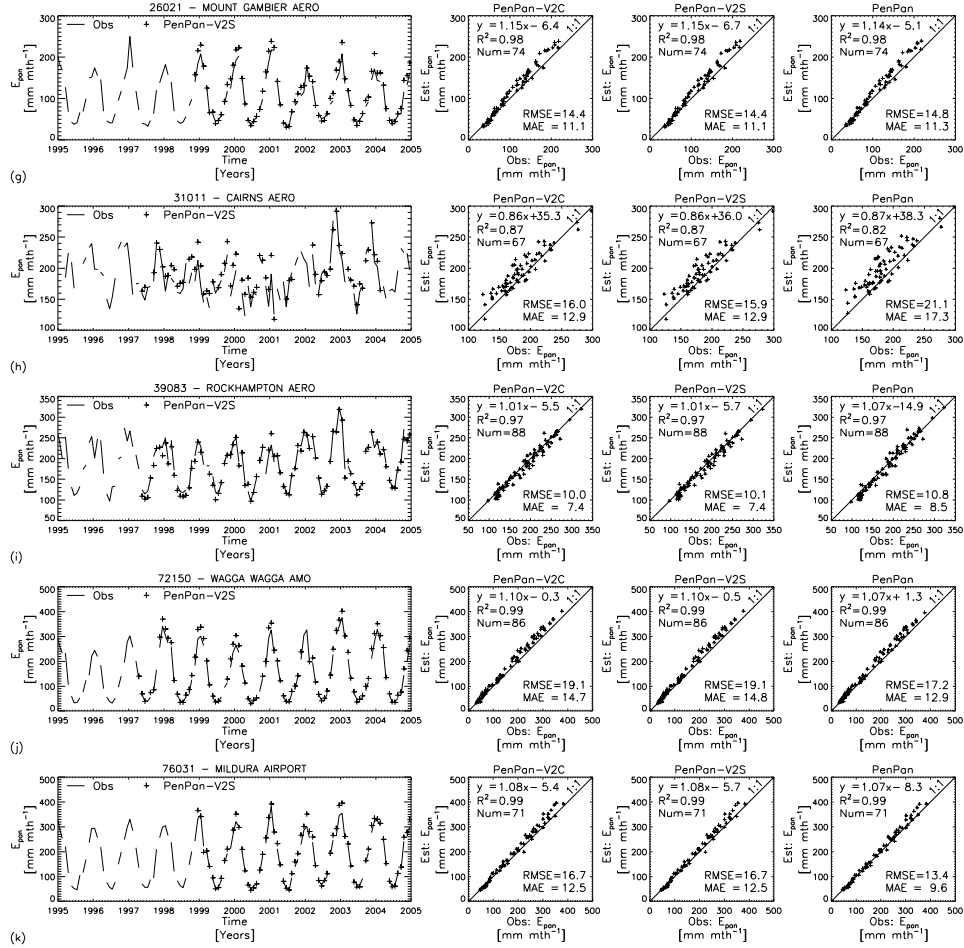


Fig. 6: (Continued).

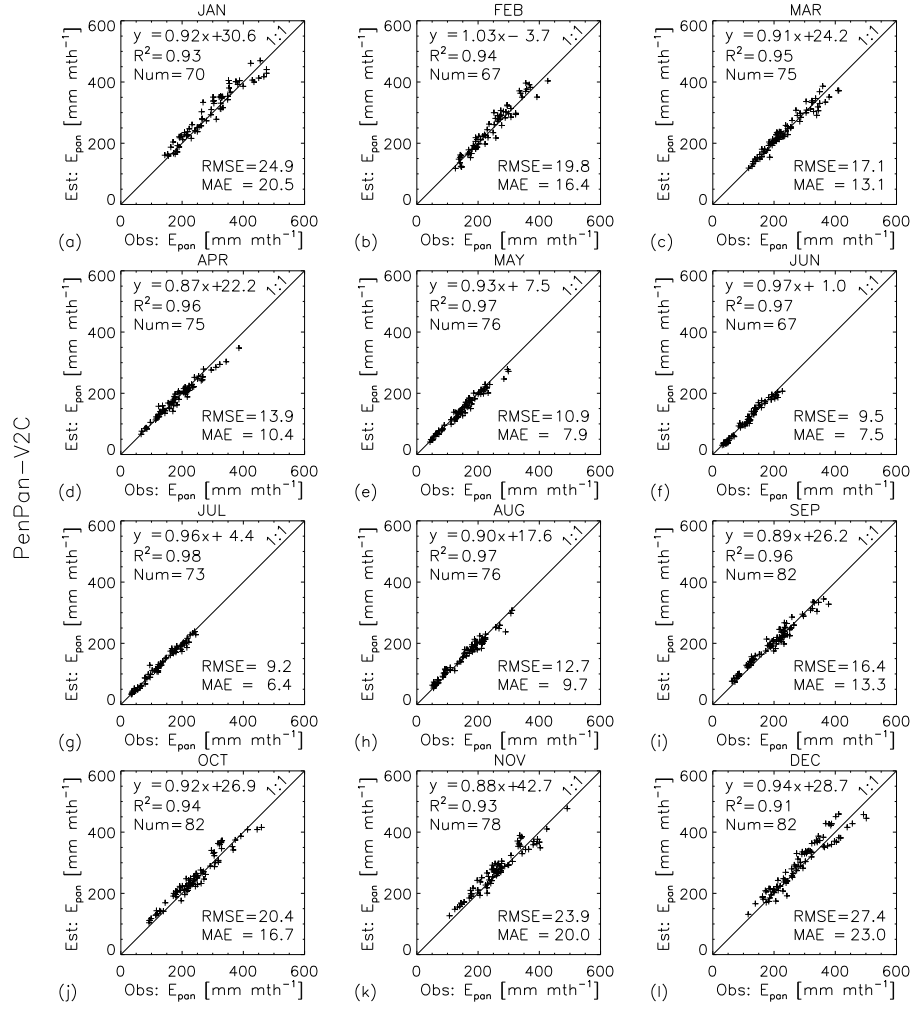


Fig. 7: Estimated E_{pan} versus observed E_{pan} over 12 separate months using all data (1:1 line shown) for the PenPan-V2C model.

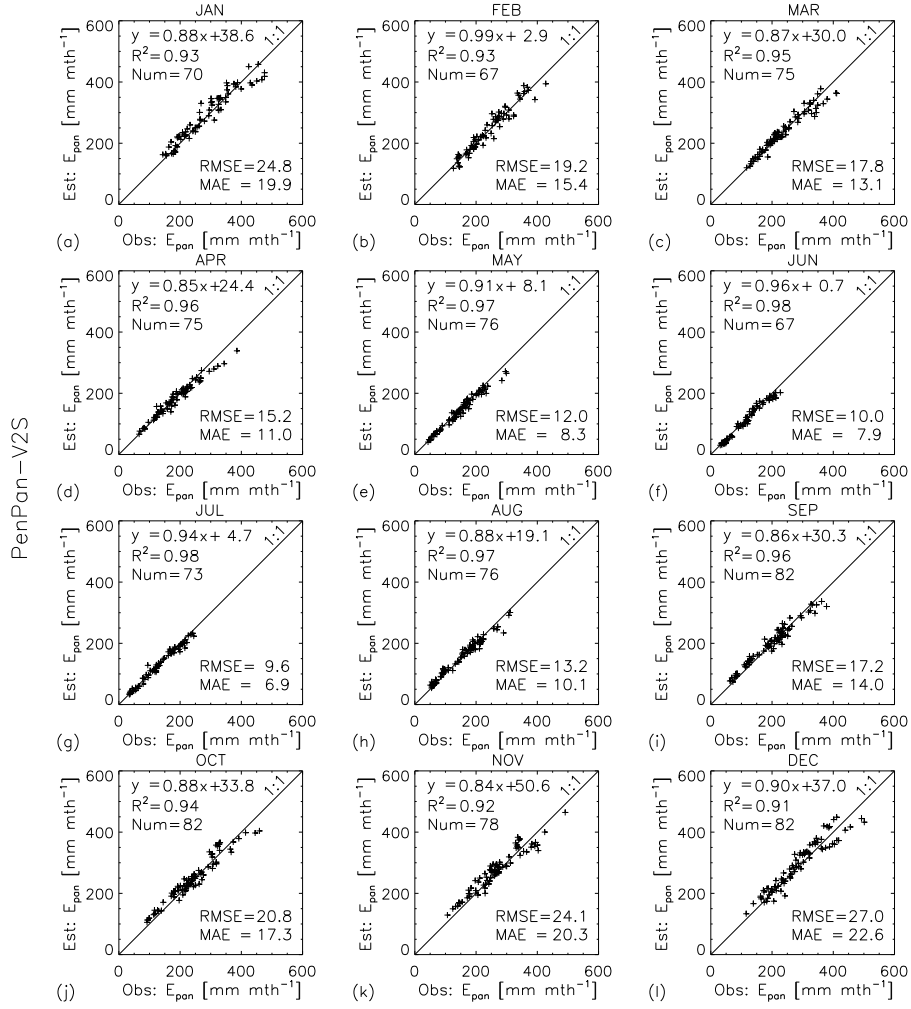


Fig. 8: Estimated E_{pan} versus observed E_{pan} over 12 separate months using all data (1:1 line shown) for the PenPan-V2S model.

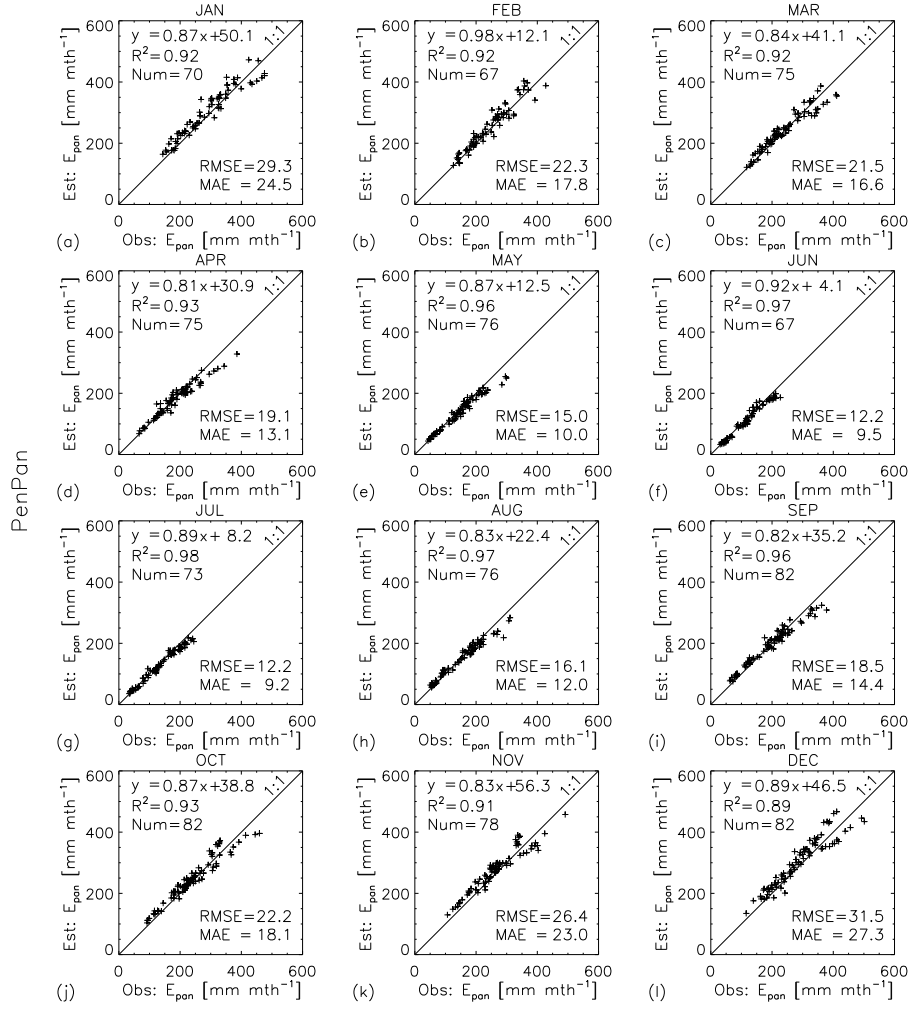


Fig. 9: Estimated E_{pan} versus observed E_{pan} over 12 separate months using all data (1:1 line shown) for the PenPan model.

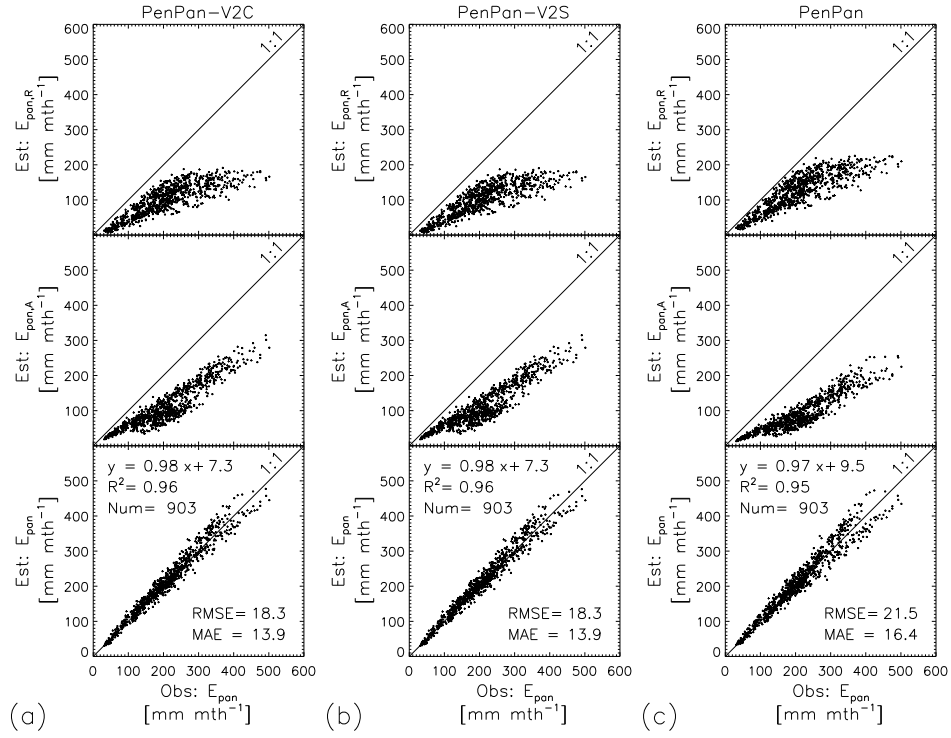


Fig. 10: Estimated $E_{pan,R}$, $E_{pan,A}$ and E_{pan} versus observed E_{pan} over monthly periods using all data (1:1 line shown): (a) PenPan-V2C, (b) PenPan-V2S and (c) PenPan models.

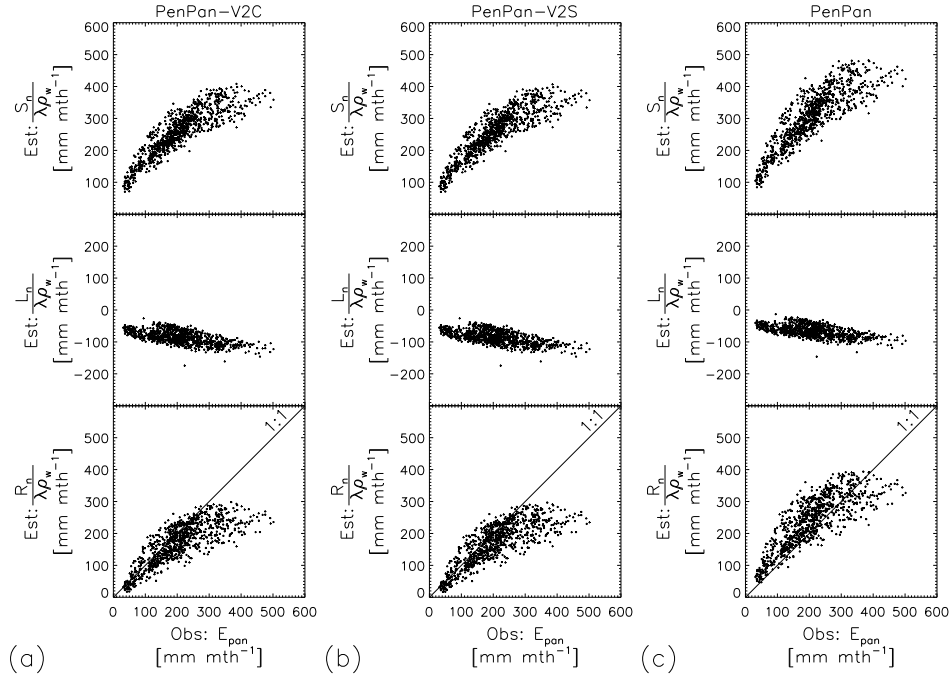
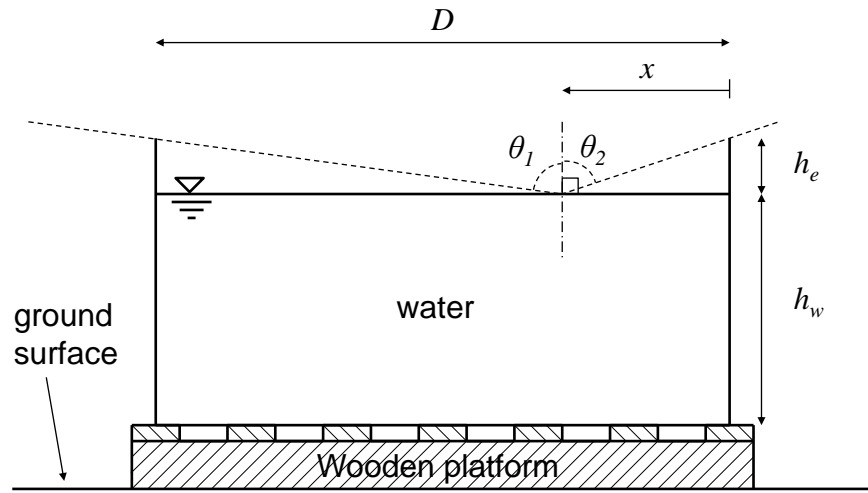


Fig. 11: Estimated $\frac{S_n}{\lambda\rho_w}$, $\frac{L_n}{\lambda\rho_w}$ and $\frac{R_n}{\lambda\rho_w}$ versus observed E_{pan} over monthly periods using all data (1:1 line shown): (a) PenPan-V2C, (b) PenPan-V2S and (c) PenPan models.



D : pan diameter, h_e : height of the rim;
 h_w : height of the water level; x : distance from the edge;
 θ_1, θ_2 : angles which pan water surface 'see' the sky.

Fig. C.1: Schematic diagram of a cylindrical pan sitting on a wooden platform. After Lim et al. (2013, their Fig. B.1).

Table 1: Key aspects of improvement in the PenPan-V2 models over the PenPan model.

	PenPan model (Rotstayn et al., 2006)	PenPan-V2 models (Current study)
1. Aerodynamic function	Empirical “wind function”.	Boundary layer theory that is parameterised using experimental results.
2. Net irradiance		
(a) Short-wave	One constant albedo and area subjected to beam and diffuse irradiance for the entire pan.	Different albedos for the pan water surface and the pan wall. Albedo and “effective” area subjected to direct irradiance vary on a monthly basis; constant albedo and area subjected to diffuse irradiance.
(b) Long-wave	Long-wave radiation exchange occurs at the pan water surface only. Assumed black body emission for the entire pan.	Long-wave radiation exchange occurs at the pan water surface and the pan wall. The pan water surface and the pan wall have different (hemispherical) emissivities.
3. Boundary conditions	Pan is full of water.	Pan is partially filled with modifications to irradiance. The temperature of the rim rapidly equilibrates with the air temperature via convection. Details in Appendix C.
4. Building blocks	Thom et al. (1981); Linacre (1994)	Lim et al. (2012, 2013)

Table 2: Details of the 11 “elite” sites (per Fig. 5) used for model evaluation.

Site	Name	Longitude	Latitude	Elevation	Data available
		[°]	[°]	[m]	[months]
3003	BROOME AIRPORT	122.23	-17.95	7	98
5007	LEARMONTH AIRPORT	114.10	-22.24	5	85
8051	GERALDTON AIRPORT	114.70	-28.80	33	98
14015	DARWIN AIRPORT	130.89	-12.42	30	88
15135	TENNANT CREEK AIRPORT	134.18	-19.64	376	68
15590	ALICE SPRINGS AIRPORT	133.89	-23.80	546	80
26021	MOUNT GAMBIER AERO	140.77	-37.75	63	74
31011	CAIRNS AERO	145.75	-16.87	3	67
39083	ROCKHAMPTON AERO	150.48	-23.38	10	88
72150	WAGGA WAGGA AMO	147.46	-35.16	212	86
76031	MILDURA AIRPORT	142.08	-34.23	50	71
Total					903

Table B.1: List of miscellaneous equations.

Equation	Reference
$\lambda = 2.501 \times 10^6 - 2370(T_a - 273.15)$	Jacobson (2005)
$s = 611 \frac{\lambda M_w}{RT_a^2} \exp \left[\frac{17.27(T_a - 273.15)}{T_a - 36.15} \right]$	Monteith and Unsworth (2008)
$\gamma = 67 - 0.0072h_z$	Linacre (1994)
$P_a = 101.3 \left(\frac{293 - 0.0065h_z}{293} \right)^{5.26} \times 10^3$	Allen et al. (1998)
$f_b = -0.11 + 1.31 \frac{S_g}{S_0}$	Roderick (1999)
$k_a = 4.1868(5.69 + 0.017(T_a - 273.15)) \times 10^{-3}$	Pruppacher and Klett (1997)
$D_h = \frac{RT_a}{M_w} \frac{k_a}{\lambda \gamma}$	By algebra.
$D_v = 2.11 \left(\frac{T_a}{273.15} \right)^{1.94} \left(\frac{P_o}{P_a} \right) \times 10^{-5}$	Pruppacher and Klett (1997)

Note:

T_a [K] is the air temperature,

M_w [kg mol⁻¹] is the molecular mass of water (=0.018 kg mol⁻¹),

R [J mol⁻¹ K⁻¹] is the ideal gas constant (=8.314 J mol⁻¹ K⁻¹),

h_z [m] is the elevation above the mean sea level,

S_g [W m⁻²] is the global solar irradiance,

S_0 [W m⁻²] is the radiation arriving at the top of atmosphere.

P_o [Pa] is the atmospheric pressure at the mean sea level (=101.3 kPa).

Table D.1: Inputs for Broome Airport (Site: 3003; December 2001).

Inputs		Value	Unit
Measurements:			
Global solar irradiance	S_g	331.668	W m^{-2}
Incoming long-wave irradiance	L_i	415.670	W m^{-2}
Air temperature	T_a	301.83	K
Wind speed at 2 m above ground level	u_2	3.05	m s^{-1}
Saturated vapour pressure at the same height at which T_a is measured	$e_s(T_a)$	3954	Pa
☼ Air vapour pressure at the same height at which T_a is measured	$e_a(T_a)$	2634	Pa
Evaporation rate	Observed E_{pan}	302.25	mm mth^{-1}
Parameters:			
Latitude	ϕ	-17.95	$^{\circ}$
Month	M	12	-
Elevation above mean sea level	h_z	7	m
Radiation arriving at the top of atmosphere	S_0	482.592	W m^{-2}
Dimensionless constant	n	0.10	-
Correction factor for the bird guard	C	1.07	-

Table D.1: (continued).

Inputs		Value	Unit
Molecular mass of water	M_w	0.018	kg mol ⁻¹
Idea gas constant	R	8.314	J mol ⁻¹ K ⁻¹
Density of liquid water	ρ_w	1000	kg m ⁻³
Pan water surface area	A_w	1.15	m ²
Area of the pan water surface subjected to diffuse irradiance	$A_{d,w}$	1.01	m ²
Area of the pan wall subjected to beam irradiance	$A_{b,wall}$	0.242	m ²
Area of the pan wall subjected to diffuse irradiance	$A_{d,wall}$	0.76	m ²
Albedo of the pan water surface subjected to diffuse irradiance	$\alpha_{d,w}$	0.08	-
Albedo of the pan wall subjected to diffuse irradiance	$\alpha_{d,wall}$	0.43	-
Albedo of the ground surface	α_{gnd}	0.20	-
Hemispherical emissivity of the water surface	ϵ_w	0.89	-
Hemispherical emissivity of the pan wall	ϵ_{wall}	0.82	-
Hemispherical emissivity of the ground surface	ϵ_{gnd}	0.90	-
Ratio of heat to mass transfer coefficients of the pan	β	1.8	-
Stefan-Boltzmann constant	σ	5.67×10^{-8}	W m ⁻² K ⁻⁴

Table D.2: Calculations for Broome Airport (Site: 3003; December 2001).

Categories	Calculations		Value	Unit
Aerodynamic function	Eq. (E.1)	P_a	101217	Pa
	Eq. (4)	f_v	9.594×10^{-11}	$\text{m s}^{-1} \text{ Pa}^{-1}$
Net irradiance	Eq. (7)	$A'_{b,w}$	1.085	m^2
	Eq. (8)	$\alpha'_{b,w}$	0.037	-
	Eq. (10)	$\tan(z)'$	0.978	-
	Eq. (11)	$\alpha'_{b,wall}$	0.495	-
	Eq. (F.1)	f_b	0.7903	-
	Eq. (6)	$S_{n,w}$	275.09	W m^{-2}
	Eq. (9)	$S_{n,wall}$	52.83	W m^{-2}
	Eq. (12)	$L_{n,w}$	-53.62	W m^{-2}
	Eq. (13)	$L_{n,wall}$	-16.37	W m^{-2}
	Eq. (5)	R_n	257.93	W m^{-2}
Evaporation rate	Eq. (B.1)	λ	2433028.4	J kg^{-1}
	Eq. (C.1)	s	227.92	Pa K^{-1}
	Eq. (D.1)	γ	66.95	Pa K^{-1}
	Eq. (2)	Estimated E_{pan}	303.1	mm mth^{-1}